

Annual Review of Astronomy and Astrophysics

The Dust Attenuation Law in Galaxies

Samir Salim¹ and Desika Narayanan^{2,3}

- ¹Department of Astronomy, Indiana University, Bloomington, Indiana 47405, USA; email: salims@indiana.edu
- ²Department of Astronomy, University of Florida, Gainesville, Florida 32611, USA; email: desika.narayanan@ufl.edu
- ³Cosmic Dawn Center at the Niels Bohr Institute, University of Copenhagen, 2100 Copenhagen; DTU-Space, Technical University of Denmark, 2800 Kongens Lyngby, Denmark

Annu. Rev. Astron. Astrophys. 2020. 58:529-75

First published as a Review in Advance on July 14, 2020

The Annual Review of Astronomy and Astrophysics is online at astro.annualreviews.org

https://doi.org/10.1146/annurev-astro-032620-021933

Copyright © 2020 by Annual Reviews. All rights reserved

ANNUAL CONNECT

www.annualreviews.org

- Download figures
- Navigate cited references
- · Keyword search
- · Explore related articles
- Share via email or social media

Keywords

ISM, dust, extinction, simulations, SED fitting, galaxy evolution

Abstract

Understanding the properties of dust attenuation curves in galaxies and the physical mechanisms that shape them are among the fundamental questions of extragalactic astrophysics, with great practical significance for deriving the physical properties of galaxies. Attenuation curves result from a combination of dust grain properties, dust content, and the spatial arrangement of dust and different populations of stars. In this review, we assess the state of the field, paying particular attention to extinction curves as the building blocks of attenuation laws. We introduce a quantitative framework to characterize extinction and attenuation curves, present a theoretical foundation for interpreting empirical results, overview an array of observational methods, and review observational results at low and high redshifts. Our main conclusions include the following:

- Attenuation curves exhibit a wide range of UV-through-optical slopes, from curves with shallow (Milky Way-like) slopes to those exceeding the slope of the Small Magellanic Cloud extinction curve.
- The slopes of the curves correlate strongly with the effective optical opacities, in the sense that galaxies with lower dust column density (lower visual attenuation) tend to have steeper slopes, whereas the galaxies with higher dust column density have shallower (grayer) slopes.

- Galaxies exhibit a range of 2175-Å UV bump strengths, including no bump, but, on average, are suppressed compared with the average Milky Way extinction curve.
- Theoretical studies indicate that both the correlation between the slope and the dust column as well as variations in bump strength may result from geometric and radiative transfer effects.

Contents	
1. INTRODUCTION	531
	531
1.2. The Importance of the Attenuation Curve for Recovering Fundamental	
·	532
2. CONCEPTS AND FORMALISM OF EXTINCTION	
	532
3. EXTINCTION CURVES: OBSERVATIONS AND EMPIRICAL	
	535
3.1. Methods of Observationally Deriving Extinction Curves	536
3.2. Empirical Properties of Extinction Curves in the Milky Way	
and Magellanic Clouds	537
3.3. Extinction Curves and External Parameters	540
3.4. Empirical Properties of Extinction Curves in Other Galaxies	541
3.5. Correcting for the Milky Way Extinction	542
4. THE THEORY OF DUST EXTINCTION LAWS	543
4.1. Extinction Law Theory: Basic Framework	543
4.2. Extinction Law Theory: Synthesis Models	543
4.3. Extinction Law Theory: Numerical Models	544
5. ATTENUATION CURVES: THEORY AND MODELING	545
	545
	546
5.3. The Origin of 2175-Å Bump Variations in Attenuation Curves	548
5.4. Theory of the IRX $-\beta$ Relation	549
8	550
6. METHODS OF OBSERVATIONALLY DERIVING DUST	
	552
	552
r	553
	555
,,	556
	558
11 /	558
8.2. Attenuation Curves of Galaxies at Redshifts Greater Than	
Approximately 0.5	
9. CONCLUSIONS	568

1. INTRODUCTION

Astrophysical dust is one of the key components of the interstellar medium (ISM) of galaxies. Dust particles (hereafter, grains) originate as a product of stellar evolution. Grains form in the atmospheres of evolved stars or remnants of supernovae and are then released or ejected into the ISM (Draine 2011), where their masses and sizes evolve owing to a diverse set of physical processes (Asano et al. 2013). Dust grains typically range in size from 5 to 250 nm (Weingartner & Draine 2001), which is two orders of magnitude smaller than household dust particles and comparable with combustion (smoke) particles. The two basic compositions of interstellar dust grains are carbonaceous, including graphite and polycyclic aromatic hydrocarbons (PAHs), and silicate.

Observationally, the presence of dust in galaxies is revealed by two general effects: (a) the production of emission in the infrared (IR) part of the spectrum, consisting of the continuum and various emission and absorption features, and (b) the modification of the stellar continuum at all wavelengths, in particular the ultraviolet (UV) to near-infrared (NIR) flux. This review focuses on understanding the driving physics and observational properties of the latter effect, encapsulated into two terms that we define in Section 1.1: extinction and attenuation. Throughout, we utilize the terminology "curves" or "laws" interchangeably to refer to the wavelength dependence of the optical depth in either extinction or attenuation. We gear this review toward general practitioners of extragalactic and galaxy evolution studies who wish to use attenuation laws to further our understanding of the physics of dust grains itself, as well as to researchers interested in using attenuation laws from a purely phenomenological perspective in order to correct the observed UV-NIR stellar emission for attenuation.

Placing this review into context, we note that Savage & Mathis (1979), Mathis (1990), and Draine (2003) reviewed the properties of extinction curves in galaxies, whereas a foundational review of dust attenuation was presented by Calzetti (2001). Here, we cover both theoretical and observational progress since these reviews, paying special attention to the details of methodology, which may prove critical for resolving some of the current conflicting results. Other aspects of dust in the ISM, including its distribution, evolution, and signatures across the electromagnetic spectrum, have been reviewed recently by Galliano et al. (2018). Steinacker et al. (2013) provide a review of dust radiative transfer methods required to model observational data. Finally, Walcher et al. (2011) and Conroy (2013) review the practice of fitting galaxy spectral energy distributions (SEDs), in which dust attenuation plays a fundamental role.

1.1. Extinction Versus Attenuation

Extinction represents the amount of light lost along a single line of sight through a dusty medium due to absorption or scattering away from the line of sight. The observational determination of extinction requires backlights such as stars, gamma-ray bursts (GRBs), quasars, or other objects with much smaller angular extent than a galaxy. The extinction at a given wavelength results from a combination of the grain size distribution and the optical properties of the grains (which is itself dependent on the chemical composition of the grains). The extinction scales with dust column density.

Although the terms extinction and attenuation are sometimes used interchangeably in the literature, there exist important conceptual differences between the two. In contrast to extinction, attenuation includes the effects arising from the distribution of stars and dust in the galaxy. Attenuation includes the same mechanisms for loss of photons as extinction, plus scattering back into the line of sight, as well as the contribution to the light by unobscured stars. **Figure 1** schematically summarizes the differences between extinction and attenuation.

Extinction: the amount of light lost along a single sightline due to absorption or scattering away from the line of sight

Attenuation: net loss of light from multiple sightlines from: extinction, scattering back into the line of sight, and contribution from unobscured stars

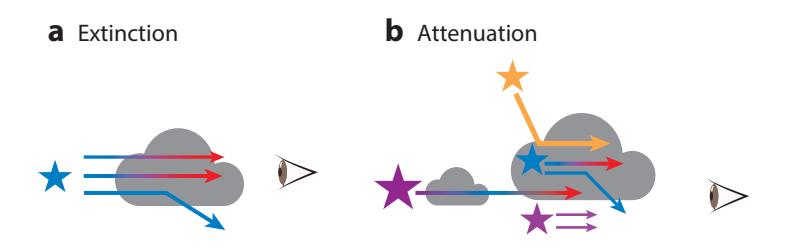


Figure 1

Schematic summarizing the difference between (a) extinction and (b) attenuation. The former encapsulates absorption and scattering out of the line of sight, whereas the latter folds in the complexities of star-dust geometry in galaxies, and may include scattering back into the line of sight, varying column densities/optical depths, and the contribution by unobscured stars.

1.2. The Importance of the Attenuation Curve for Recovering Fundamental Physical Properties of Galaxies

To demonstrate the importance of the dust attenuation curve in deriving the physical properties of galaxies, we conduct a simple experiment by generating mock SEDs from z=0 galaxies formed in a cosmological hydrodynamic simulation (the SIMBA model; Davé et al. 2019), and then fitting the SEDs with the Bayesian SED fitting software PROSPECTOR (Leja et al. 2017, 2018; Johnson et al. 2019). We fit the SEDs using *Galaxy Evolution Explorer* (GALEX) and *Hubble Space Telescope* (HST) photometry, along with the optional addition of *Herschel Space Observatory* IR photometry. When including the IR photometry, we allow the IR SED to be modeled freely. We assume a τ -model star-formation history, and vary only the assumed attenuation curve, employing either a Calzetti et al. (2000) curve or an average Small Magellanic Cloud (SMC) extinction curve. We show the comparison between the derived stellar masses and star-formation rates when varying only the assumed attenuation curve in **Figure 2**. The derived physical properties can vary dramatically, depending on the assumed dust attenuation curve in SED fitting, a point that has been amplified in the observational literature (e.g., Kriek & Conroy 2013, Reddy et al. 2015, Shivaei et al. 2015, Salim et al. 2016).

2. CONCEPTS AND FORMALISM OF EXTINCTION AND ATTENUATION CURVES

There are diverse formalisms and parameterizations that are used to present and describe dust extinction curves, and, by extension, dust attenuation curves. In this review, we use a scheme that builds upon intuitive concepts, but we also list some of the traditional measures or quantities for completeness. In this section, concepts referring to attenuation and attenuation curves and to extinction and extinction curves can be used interchangeably.

If $m_{\lambda,0}$ is an intrinsic, unattenuated SED of some astronomical object expressed in magnitudes, where wavelength λ spans a range from the Lyman limit (912 Å) to the tail of stellar emission (\sim 5 µm), and m_{λ} is the observed, attenuated SED, then

$$A_{\lambda} = m_{\lambda} - m_{\lambda,0} \tag{1}$$

represents the wavelength-dependent attenuation in magnitudes. We can think of A_{λ} as consisting of a normalization (e.g., A_{λ} at $\lambda \approx 5500$ Å; A_{V}), and a shape (e.g., A_{λ}/A_{V}). It is the shape of the curve that is generally referred to as the attenuation/extinction curve/law. Thus, if two galaxies, one with $A_{V}=0.1$ and another with $A_{V}=1$, have the same A_{λ}/A_{V} , they are said to have the same

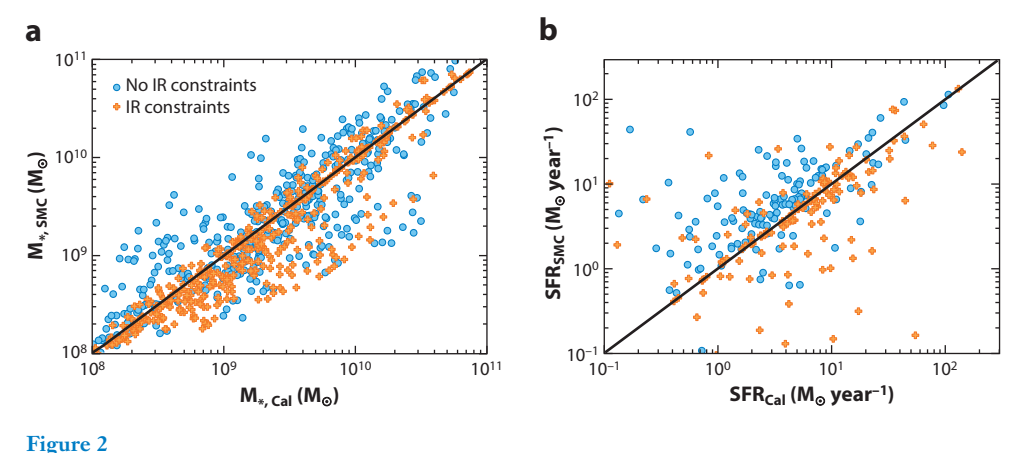


Figure 2

Results from fitting the mock SEDs of galaxies formed in a cosmological hydrodynamic simulation, but assuming either a Calzetti et al. (2000) attenuation curve in the fits (abscissa) or an SMC extinction curve (ordinate). Shown are (a) a comparison of derived stellar masses and (b) a comparison of the derived star-formation rates. The colors denote whether the SED fits included IR constraints (orange) or not (blue). Panel b excludes fully quenched galaxies. The derived physical properties of galaxies are strongly dependent on the assumed attenuation curve and highlight the importance of the attenuation curve in modeling the physical properties of observed galaxies. The calculations for this figure were performed by Sidney Lower (University of Florida), and the authors request that any reproduction of this image attribute credit to her. Abbreviations: SED, spectral energy distribution; SFR, star-formation rate; SMC, Small Magellanic Cloud.

attenuation curve because their shapes are the same. What is different is the normalization, which typically arises from different column densities of dust.

Curves are often expressed normalized by A_V , though the choice of wavelength or band used for normalization is arbitrary. Older literature often expressed curves normalized by reddening $[A_B - A_V \equiv E(B - V)]$ and denoted them as k_λ [meaning that $k_V \equiv R_V$, since $R_V = A_V/(A_B - A_V)$]. Reddening-normalized curves can be converted into A_λ/A_V normalization and vice versa (they contain identical information), but the interpretation of the former is less intuitive because the slopes in the optical range (between B and V) are identical for all curves by definition. A more physically motivated but less practical normalization would be by dust column density or its proxy, such as the H column density (e.g., Mathis et al. 1977).

Detailed individual curves contain a wealth of information that is difficult to assimilate and compare from one curve to another solely by looking at the plots of A_{λ}/A_{V} against λ . It is therefore useful to define certain parameters of the curves. In this review, we focus on two principal and three additional features, whose definitions are shown schematically in **Figure 3**, where we use the average Milky Way (MW) extinction curve as an example. Broadly, we define five regimes: the overall UV–optical slope, UV slope, optical slope, near-IR slope, and the UV (2175-Å absorption) bump strength. These parameters are independent of how A_{λ} is normalized and are mostly not based on any mathematical parameterization of the curve, which makes them more universal (we discuss a functional parameterization of attenuation curves in Section 7).

As a general high-level characterization of a curve, it is useful to define its overall UV–optical slope, which we take to be the ratio of extinctions at 1500 $\rm \mathring{A}$ and in the V-band:

$$S \equiv A_{1500}/A_V$$
 (UV-optical slope).

UV-optical slope: $S \equiv A_{1500}/A_V$

UV slope:

 A_{1500}/A_{3000}

Optical slope: A_B/A_V

Near-IR (NIR) slope: β_{NIR} where $A_{\lambda}/A_{V} = \left(\lambda/5500 \text{ Å}\right)^{-\beta_{\text{NIR}}}$

UV (2175-Å absorption) bump strength: $B \equiv A_{\text{bump}}/A_{2175}$

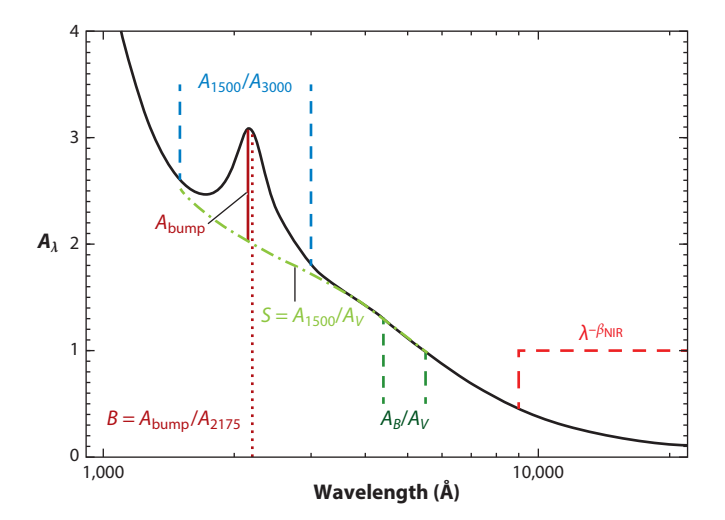


Figure 3

Schematic representation of an attenuation or extinction curve and the parameters to describe and quantify it (we use the Fitzpatrick 1999 average Galactic extinction curve as our example). The attenuation or extinction curve is the shape of A_{λ} versus wavelength, irrespective of its normalization. Shown here is a nonnormalized curve, so the values on the y axis are arbitrary. The parameters whose definitions are illustrated are the UV slope, the strength of the UV bump (B), the optical slope (directly proportional to $1/R_V$), and the NIR power-law slope ($\beta_{\rm NIR}$). The UV-optical slope (S) is defined over the range shown in green.

The shorter wavelength corresponds to the far-UV (FUV) wavelength traditionally used as a star-formation rate (SFR) indicator or in the calculation of the IR excess (IRX). The attenuation through the GALEX FUV bandpass (A_{FUV}) is on average 0.03 mag higher than at 1500 Å. If we assume that attenuation curves are well modeled by a power law between 1500 and 5500 Å, the exponent of the curve $A_1/A_V = (\lambda/5500 \text{ Å})^{-n}$ would be directly related to the UV-optical slope via

$$n = 1.772 \log S$$
, 3.

though note that the use of S does not imply that the curve follows a power law. Power-law parameterization requires caution because real curves often depart significantly from it, so forcing a power-law fit will be sensitive to the exact range of wavelengths, sampling, and the treatment of the UV bump. We stress that curves tend to be distributed more uniformly in n (i.e., $\log S$) than in S, so an appropriate way to average UV-optical slopes in some sample is by using a median or a geometric mean of S values.

The second principal parameter is the strength of the UV bump, which we define as the ratio of extra extinction due to the bump at 2175 Å (A_{bump} ; the amplitude above the baseline) to the total extinction at 2175 Å (A_{2175}):

$$B \equiv A_{\text{bump}}/A_{2175}$$
 (UV bump strength), 4.

which is illustrated in **Figure 3**. The UV bump strength can formally take a value between 0 (no bump) and 1 (all extinction at 2175 $\rm \mathring{A}$ is due to the bump). The baseline extinction (i.e., the extinction in the absence of the bump) can be estimated by interpolating the extinction shortward and longward of the bump, for example, using

$$A_{2175,0} = 0.33A_{1500} + 0.67A_{3000},$$
 5.

which we determined empirically using simulated attenuation curves from Narayanan et al. (2018a). The definition of the bump used in this review is based on normalizing the bump at the same grain size (and therefore wavelength), so it is more physically motivated than normalizing A_{bump} by A_V or by $A_B - A_V$ (the latter is often called E_b). Although parameterization of the bump also includes its width and the central wavelength (e.g., Noll et al. 2009b, Conroy et al. 2010, Narayanan et al. 2018a), information on these parameters is very limited in the case of most observed attenuation curves. Also it has so far proven difficult to relate them to dust physics even in the case of extinction curves (Fitzpatrick & Massa 1986, Cardelli et al. 1989), so we do not include them among the parameters discussed here.

In addition to these two principal parameters, for a more detailed study of extinction and attenuation curves it is also useful to define slopes in specific wavelength ranges. We define the UV slope as the ratio of monochromatic extinctions at $1500\,\text{Å}$ and $3000\,\text{Å}$:

$$A_{1500}/A_{3000}$$
 (UV slope), 6.

where the longer wavelength corresponds to the shortest wavelength not affected by the UV bump. We define the optical slope of the curve as

$$A_B/A_V$$
 (optical slope), 7.

i.e., the ratio of extinctions in B and V bands, which agrees with the ratio of monochromatic extinctions at 4400 and 5500 Å to within 1.5% for a wide range of galaxy SEDs. The optical slope is directly related to the traditional ratio of total to selective extinction (R_V), as

$$A_B/A_V = 1/R_V + 1.$$
 8.

 A_B/A_V is more intuitive than R_V , with the added benefit that it is directly related to the normalization of A_λ used in the modern literature.

Following the practice in the literature, the NIR slope of the extinction curve is defined as the value of the power-law exponent, β_{NIR} :

$$A_{\lambda}/A_{V} = (\lambda/5500 \text{ Å})^{-\beta_{\text{NIR}}}$$
 (NIR slope), 9.

which best describes the curve in the NIR wavelength range, usually starting around 0.9 μ m and extending to 2–5 μ m, depending on the available data.

3. EXTINCTION CURVES: OBSERVATIONS AND EMPIRICAL PROPERTIES

Extinction curves are the building blocks of attenuation curves, and a complete understanding of the latter requires understanding of the former. Any variation in the extinction curve between galaxies would also drive variations in the observed attenuation curves. Because the sources of light (stars) and the places where it is scattered and absorbed (ISM) can have a complex arrangement, it is nontrivial to map an extinction curve into an effective attenuation curve, and the two differ in ways that are difficult to systematize observationally (Hagen et al. 2017, Corre et al. 2018). Theoretical simulations have shown that, for a fixed extinction curve, the varying dust content and the complexities of the star–dust geometry in galaxies result in a diverse range of attenuation curves (e.g., Narayanan et al. 2018a, Trayford et al. 2020; Section 6).

3.1. Methods of Observationally Deriving Extinction Curves

The best constraints on extinction curves come from the Galaxy and the Magellanic Clouds. Here, we review how the extinction law is determined in these systems; results and methods regarding more distant galaxies are covered separately in Section 3.4.

Every method for the determination of extinction curves requires observations of point sources affected by dust and their comparison to reference spectra or SEDs that are dust free. The reference spectra can be either empirical or based on theoretical models. There are two principal approaches, especially when it comes to the study of the MW extinction curve: the use of individual stars (the pair method), and, more recently, the statistical (or survey) method, which uses a large number of stars.

The pair method has a long history dating back to Stebbins et al. (1939), who used pairs of B stars to establish that the extinction curve in the optical region follows roughly a λ^{-1} dependence. The pair method consists of comparing a reddened star with a star of the same (or nearly the same) spectral type and luminosity class that is largely dust free. Stars of type O6-B5 and luminosity classes III-V are most suitable because of relatively constant intrinsic colors (Fitzpatrick & Massa 1986).

If the distances to both stars in a pair were known, and if the comparison star was truly dust free, obtaining A_{λ} in different bands would be trivial. Because accurate distances in the general case are not known, the usual approach is to assume that extinction approaches zero at infinite wavelength. This anchoring will to some extent be sensitive to the method of extrapolation from the longest available wavelength to infinite wavelength, so it is useful to use data extending as far into the NIR as possible, while avoiding potential circumstellar dust (Savage & Mathis 1979).

If NIR data are absent, which was the case in early studies in particular, one can only obtain a relative extinction curve—extinctions with respect to some band (e.g., $A_{\lambda} - A_{V}$), derived by comparing the colors of a reddened and a dust-free star, and typically normalized by $A_{B} - A_{V}$ (e.g., Massa & Fitzpatrick 1986). Relative curves are useful for establishing the characteristics of local features—for example, the position and the width of the UV bump—but cannot be used to obtain the parameters required to characterize and compare the curves discussed in Section 2, except for $\beta_{\rm NIR}$.

One limitation of the empirical pair method is that comparison stars may also suffer from some dust extinction that needs to be corrected (Massa et al. 1983), meaning that the pair method is of little value to study the extinction curve of low-opacity (high Galactic latitude) sightlines. This limitation can be overcome by using theoretical stellar atmosphere models as dust-free references, which also has the advantage that the extrapolation of NIR extinction is not needed to anchor the curves (Fitzpatrick & Massa 2007).

Another method to map extinction curves across the sky, including high-latitude sightlines, is to use a large-survey, statistical approach. For example, Peek & Graves (2010) used red-sequence galaxies from the Sloan Digital Sky Survey (SDSS) as "standard crayons," whose intrinsic colors are known. Schlafly et al. (2010) utilized the fact that the main sequence turnoff for field stars (old populations) has a sharp blue edge, which can be accurately determined from a large SDSS sample of stars lying between 1 and 8 kpc. Subsequently, Schlafly & Finkbeiner (2011) used spectroscopic parameters of SDSS Sloan Extension for Galactic Understanding and Exploration (SEGUE) stars to predict stellar colors based on models. Berry et al. (2012) used SED fitting to expand the standard crayon method to a general population of stars from SDSS and the Two-Micron All Sky Survey (2MASS). Schlafly et al. (2014, 2016) also used optical–NIR SED fitting, but as a function of spectroscopically determined temperature and metallicity. Wang & Chen (2019) used the relatively constant colors of red clump stars to get extinctions.

3.2. Empirical Properties of Extinction Curves in the Milky Way and Magellanic Clouds

In discussing the empirical properties of extinction curves in the Galaxy and Magellanic Clouds, there are two common threads that emerge: (a) Extinction curves can vary significantly from one line of sight to another within the same galaxy, and (b) average extinction curves differ, sometimes dramatically, from one galaxy to another. The first point is illustrated in **Figure 4a**, which shows the average MW extinction curve together with a wide band of extinction curves to individual sightlines in the MW, which all exhibit a UV bump (Section 3.2.2). The second thread was recognized already in early studies with the *International Ultraviolet Explorer* (IUE) that showed that the Large Magellanic Cloud (LMC) and in particular the SMC have on average steeper and less bumpy curves (**Figure 4**), and has been amplified in the literature over the past decade with major HST campaigns (e.g., Sabbi et al. 2013, De Marchi et al. 2016, Yanchulova Merica-Jones et al. 2017, Roman-Duval et al. 2019).

3.2.1. Extinction curve slopes in the UV and optical. One of the main questions in the study of extinction is whether curves to different sightlines in the MW (and more generally) belong to a single-parameter family of curves, meaning that specifying a slope in one spectral region would determine the full curve.

The idea that the slopes over different wavelength ranges, from 1200 Å to ~1 μ m, are correlated was first suggested by Cardelli et al. (1989, hereafter CCM). These authors took relative UV extinction curves toward 31 significantly reddened Galactic plane stars from Fitzpatrick & Massa (1988) and appended them with optical and NIR photometry to obtain absolute extinction curves. Specifically, they showed that the slopes between different wavelengths (in particular the UV wavelengths) and $V(A_{\lambda}/A_{V})$ are correlated with the optical slope $R_{V}^{-1} (\equiv A_{B}/A_{V} - 1)$. Based on this, they presented an R_{V} -dependent parameterization of curves that is still widely used and is referred to by Cardelli et al. as the mean extinction law (for a given optical slope). The caveat regarding the mean relation, already acknowledged by Cardelli et al., is that though different slopes are correlated with the optical slope, the scatter around the mean relation at any given value of optical slope is greater than the observational errors (in particular at $\lambda < 1400 \text{ Å}$), suggesting more complex underlying diversity.

Although the existence of the correlation between UV and optical extinction curves within the Galaxy is generally accepted, Fitzpatrick & Massa (2007) brought it into question by pointing out that by normalizing both the UV and optical slopes at V, Cardelli et al. may have introduced an artificial correlation even if there was none to begin with. Although this concern is valid in general, it is not clear that the uncertainties in this case are such to remove the genuine correlation. To demonstrate this, in **Figure 4**b we show a pure UV slope defined between two points in the UV (1500 and 3000 Å), not with respect to V, against the optical slope A_B/A_V . Data for the \sim 70 stars come from Fitzpatrick & Massa (1990, 2007). A relatively narrow relation emerges, confirming the original CCM relation (overplotted in **Figure 4**b).

The single-parameter family picture that emerged from traditional (low Galactic latitude) MW sightlines does not extend to the Magellanic Clouds. Early studies by Nandy et al. (1981), Koornneef & Code (1981), Clayton & Martin (1985), and Fitzpatrick (1985) found that, though there was significant regional variation in the curve across the LMC, on average the LMC had a UV curve steeper than that of the MW, especially in the 30 Doradus star-forming complex. Similarly, early studies of the SMC (e.g., Prevot et al. 1984, Gordon & Clayton 1998) found even steeper UV slopes. In short, though the optical extinction curve slopes for the LMC and the SMC fall within the range of MW sightlines, the UV slopes tend to be significantly steeper (Figure 4b),

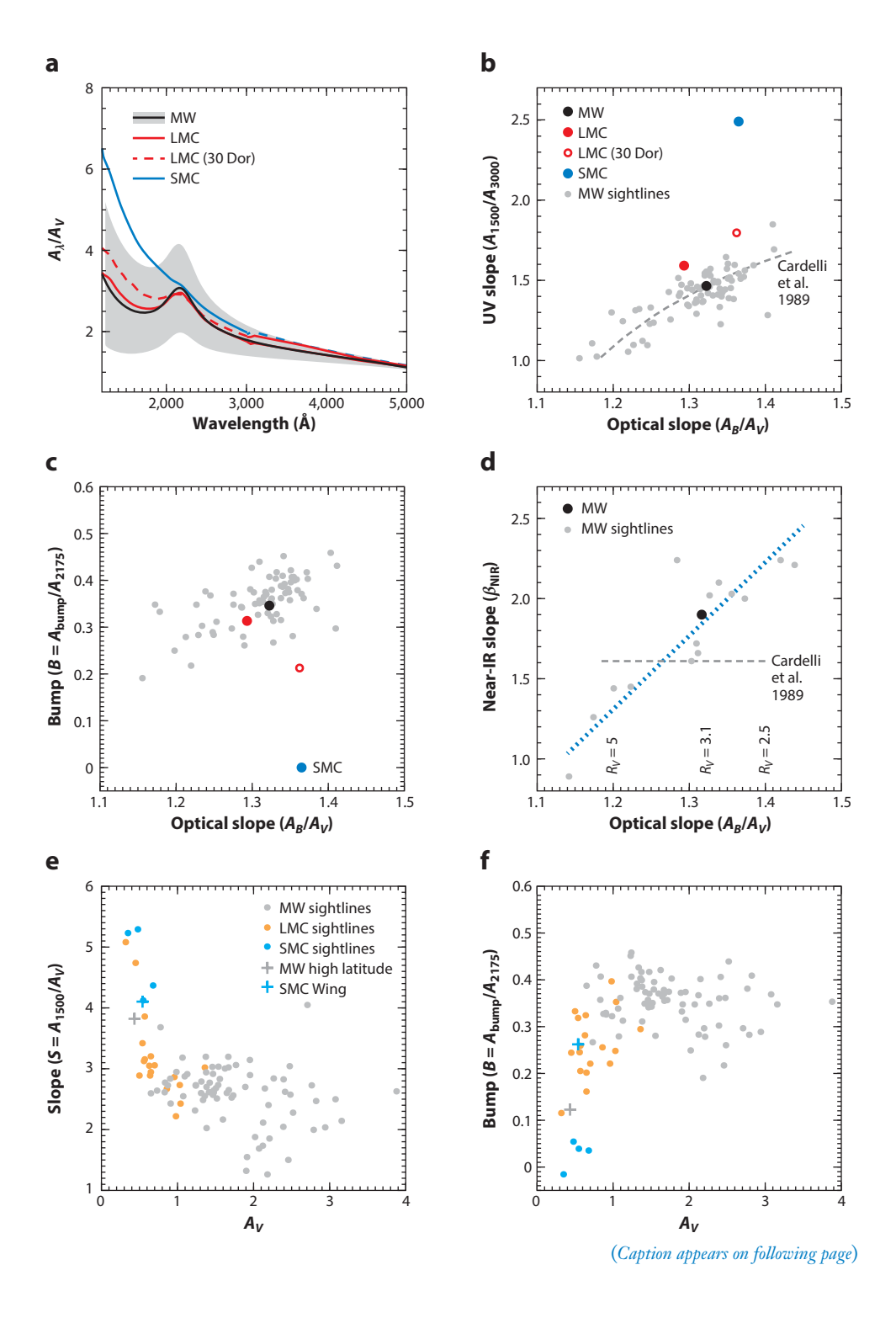


Figure 4 (Figure appears on preceding page)

The empirical properties of average extinction curves of the MW (black), LMC (red), and SMC (blue), as well as of individual sightlines within the MW (gray band and dots), LMC (orange), and SMC (light blue). Panel a shows A_V -normalized extinction curves. Panels b-d show the UV slope, bump strength, and near-IR slope, respectively, against the optical slope, with the Cardelli et al. (1989) relation overplotted in panels b and d and the linear fit in panel d. Correspondence between A_B/A_V and R_V is shown in panel d. Panels e and f show the overall slope and bump strength, respectively, versus optical depth, with high-latitude MW sightline to HD 164340 (gray cross) and SMC Wing sightline (blue cross) added. MW data were based on Fitzpatrick & Massa (1990, 2007, 2009), Fitzpatrick (1999), Clayton et al. (2000), and Nataf et al. (2016), and SMC/LMC data were taken from Gordon et al. (2003). Abbreviations: LMC, Large Magellanic Cloud; MW, Milky Way; SMC, Small Magellanic Cloud.

highlighting the limitation of characterizing curve slopes with R_V alone. One can ask whether individual lines of sight within the LMC and SMC obey some other relationship, offset from that of the MW, but the current data are not of sufficient accuracy, nor do the LMC/SMC sightlines have a sufficiently wide range in optical slopes, to provide a definitive answer (Gordon et al. 2003). From a practical standpoint, the shapes of LMC and SMC curves imply that the CCM R_V -dependent mean curves, or their updates and equivalents (O'Donnell 1994, Fitzpatrick 1999, Valencic et al. 2004), cannot straightforwardly be used for accurate modeling or parameterization of extinction/attenuation curves in general (see also Section 7).

3.2.2. The 2175-Å UV bump. The UV bump (Stecher & Donn 1965) represents a prominent feature in the extinction curves of the MW and LMC, spanning roughly the wavelength range between 1700 and 2700 Å. A systematic study on the observational properties of the bump toward many sightlines in the MW carried out by Fitzpatrick & Massa (1986) revealed that the peak wavelength of the bump is variable, but the deviations from 2175 Å are relatively small ($1\sigma \approx 5$ Å). Furthermore, the width of the bump in the Galaxy (FWHM = 480 Å, on average) was also found to be variable, with 1σ variations of \approx 20 Å. Broad bumps tend to be associated with denser environments (as assessed visually). The original Fitzpatrick & Massa (1986) Galactic study determined that the peak wavelength and the width of the bump are not correlated with each other, and neither is correlated with the slope of the extinction curve (Cardelli et al. 1989).

The feature of the bump that has a greater practical significance is its strength. Cardelli et al. (1989) showed that the extra extinction in Galactic sightlines due to the bump, when normalized by A_V , is correlated with the optical slope of the extinction curve (R_V^{-1} or A_B/A_V), such that the steeper slopes have stronger bumps. In **Figure 4c**, we revisit this result, but normalize the bump amplitude to the extinction at 2175 Å, which removes any spurious correlation between the axes. MW sightlines show a spread of a factor of two in UV bump strength (the average curve has $B_{\rm MW} = A_{\rm bump}/A_{2175} = 0.35$), and a correlation with the optical slope is present. Thus, the UV bump fits the scheme of a single-parameter family of extinction curves, at least in traditional, high-reddening MW sightlines. However, the LMC 30 Dor average curve has an ~50% weaker bump than MW sightlines of the same A_B/A_V , whereas the SMC average curve has essentially no bump (Prevot et al. 1984, Gordon & Clayton 1998, Misselt et al. 1999, Gordon et al. 2003). Exceptions to this general pattern are discussed in Section 3.3.

3.2.3. Extinction curve slopes in the near-IR. Historically, the properties of the NIR extinction curve have been more challenging to study than those of the UV and optical curves due to the lack of data and low extinctions. Cardelli et al. (1989) argued for a universal NIR extinction law at $\lambda > 0.9 \,\mu\text{m}$, so in their parameterization the NIR power-law slope is fixed to $\beta_{\text{NIR}} = 1.61$, based on the curve of Rieke & Lebofsky (1985). This value is no longer favored for the average

MW curve. A range of higher values has been found in various recent studies, as summarized by Wang & Chen (2019), who used a survey approach to find a typical value of $\beta_{\rm NIR} = 2.07$. This value agrees with Nataf et al. (2016), who found an average $A_V/A_{K_c} = 13.4$ ($\beta_{\rm NIR} = 1.90$). To reveal any trends between individual sightlines, Fitzpatrick & Massa (2009) used theoretical stellar atmosphere models to obtain, independent from one another, the optical and NIR extinction curves of 14 stars. The power-law slopes span a range from 0.9 to 2.3, i.e., extending on both sides of the traditionally used values, and agree with recent high values at $R_V = 3.1$. Interestingly, though the number of data points is small, their NIR slopes show a general trend with the optical slopes, as shown in **Figure 4d** and given by the relation

$$\beta_{\text{NIR}} = 4.59(A_B/A_V) - 4.20.$$
 10.

Thus, rather than being universal, the NIR extinction curve appears to be part of a single-parameter family, at least for the MW sightlines. The shapes of the NIR extinction curves of the LMC and SMC are not well known.

3.3. Extinction Curves and External Parameters

So far, we have reviewed and examined correlations between the internal features of extinction curves, finding trends for traditionally studied MW sightlines, but not extending to the LMC/SMC average curves. One could ask if there existed an external parameter that could explain the diversity of curves both within the MW and between the MW and LMC/SMC sightlines, so as to lead to a continuum of dust properties, as suggested by Clayton et al. (2000) and Gordon et al. (2003). In addressing this question, we focus on the two features that show the greatest diversity—the overall UV-optical slope (S) and the bump strength (B)—and explore how they relate to three potential proxies of dust column density $(A_{1500}, A_V, A_R - A_V)$, gas column density [N(H_I)], and two variants of the gas-to-dust ratio [N(H_I)/ A_V and N(H_I)/($A_B - A_V$)]. We find the strongest trends against optical opacity (A_V) , so in **Figure 4e,f**, we show individual sightlines in the MW, LMC (including 30 Dor region), and SMC (LMC/SMC data from Gordon et al. 2003). Particularly noteworthy is the fact that though the LMC and SMC sightlines, on average, exhibit steeper curves and smaller bumps than the Galaxy, they are also far more transparent than typical MW sightlines. Remarkably, in regions where the MW and LMC A_V values overlap, the slopes are similar. Can the gap between the MW and SMC also be bridged? This question motivated Clayton et al. (2000) to study high-latitude, low-opacity sightlines in the MW. Their least reddened sightline ($A_V \sim 0.4$, HD 164340; shown in **Figure 4e**) has a slope steeper than most LMC sightlines and almost as steep as some SMC ones, plus a nearly absent bump, like typical sightlines in the SMC. Similarly, the extinction curve toward the SMC Wing, a more quiescent and gas-poor sightline, has a bump as strong as many MW sightlines and a relatively shallow UV slope (a number of other sightlines in the SMC show evidence for a weak UV bump, albeit in attenuation curves; Hagen et al. 2017). Furthermore, the slopes appear to be weakly correlated with A_V even for high-opacity MW sightlines. Trends similar to those described here exist between the UV-only slope (A_{1500}/A_{3000}) and A_V . However, the trend is not as pronounced between the optical slopes (R_V) and A_V , which is consistent with the existence of a large range of UV slopes for a given optical slope in non-MW curves, as discussed above.

The general picture emerging from both local measurements and those of distant galaxies (Section 3.4) is that extinction curves have a range of steep slopes and weak bumps for $A_V < 0.8$ but are relatively shallow and bumpy when the A_V (and therefore, presumably, metallicity) is

higher. The dependence on A_V is likely the consequence of a more fundamental dependence on the dust column density.

3.4. Empirical Properties of Extinction Curves in Other Galaxies

The study of dust extinction in extragalactic systems provides an opportunity to understand the physics driving grain size evolution and compositions in galaxies over a diverse range of environments. Much progress in this area has been made recently.

3.4.1. The Local Universe. In the Local Universe, much of our understanding of extinction curves outside of the Galaxy or Clouds comes from HST-enabled dust extinction maps in M31 that were derived using novel color–magnitude diagram fitting methods (Dalcanton et al. 2015, Dong et al. 2016). Dong et al. (2014) measured the extinction curve toward the bulge of M31 and found an optical curve steeper than the Galactic average ($R_V \approx 2.4$ –2.5). Of particular note is that HST observations of the disk in M31 reveal an extinction curve having comparable slope with the Galactic mean, though with possibly weaker bump (Bianchi et al. 1996). These results, taken together, hint at common trends in the extinction curves in the MW and M31.

3.4.2. High redshift. Given that the dust extinction law is dependent on grain size distribution and composition, we might expect it to vary not only with environment but even among galaxies of a similar mass but at different redshifts, as different processes (i.e., growth via metal accretion, coagulation, shattering, or sputtering) may dominate at different times and in different environments. Similarly, different dust production processes may dominate at early times, and the detections at z > 6 may place constraints on both formation and growth mechanisms (e.g., Draine 2009, Riechers et al. 2013, Strandet et al. 2017, Marrone et al. 2018). Because of this, there has been significant interest in characterizing the dust extinction law at high redshift. Due to typically subsolar metallicity in high-redshift galaxies, an SMC-like extinction curve is often invoked. This said, as in low-redshift studies, the extinction law is found to have a range of slopes and bump strengths among the disparate populations studied over a broad range of cosmic time at high redshift.

Typically, one needs a backlight to produce an absorption spectrum from which to infer an extinction curve. Common sources include GRB afterglows, due to their relatively well-characterized spectra, and quasars (e.g., York et al. 2006, Stratta et al. 2007). Other groups have taken advantage of magnitude differences at different wavelengths in image pairs of lensed systems to derive extinction laws (e.g., Malhotra et al. 1997, Falco et al. 1999, Muñoz et al. 2004), a method developed by Nadeau et al. (1991).

Of particular interest in high-redshift studies of the extinction curve have been potential variations in the 2175-Å UV bump. High-z galaxies provide a particularly useful laboratory to study the bump strength owing to the diverse range of metallicities and incident radiation fields. Schady et al. (2012) studied the mean curve of 17 GRB host galaxies and found SMC-like curves with minimal UV bump strengths. Zafar et al. (2011) use a relatively homogeneous sample of 41 GRB afterglows and find UV bumps to be present in only three cases, which were all associated with $A_V > 1$. The general absence of bumps was confirmed more recently by Zafar et al. (2018), where all GRB extinction curves for which the bump region was observed were featureless (and all had $A_V < 0.3$). These same studies have shown that the majority of GRB extinction curves share the steep UV-optical slope of the SMC curve, and like the SMC curve they are typically associated with low columns of dust ($A_V < 0.5$). Shallow UV-optical slopes similar to that of the MW were typically found in high- A_V sightlines, highlighting the connection between A_V

and slopes, suggested by Schady et al. (2012) and discussed in Section 3.3. Turning to other techniques, Motta et al. (2002) confirmed the presence of a UV bump in a $z \sim 1$ lens galaxy. In contrast, however, York et al. (2006) find no UV bump and an SMC-like slope in the mean extinction curve of \sim 800 SDSS quasar absorbers at 1 < z < 2. Note that these absorbers tend to have quite low optical depth ($A_V < 0.3$). A special search targeting absorbers that exhibit a UV bump showed that such cases do exist. Out of \sim 30,000 absorbers toward quasars selected in the SDSS at $z \sim 1.0$ –2.2, Ma et al. (2015, 2017) identified 14 cases in which the UV bump was present, including many that have bumps as large as the Galactic mean.

3.5. Correcting for the Milky Way Extinction

The Galactic extinction curve is routinely used to correct the fluxes of extragalactic observations. Several open questions are related to this procedure. How should we construct maps of reddening $(A_B - A_V)$ from which extinctions are derived? Is it appropriate to use an average extinction curve (fixed R_V), neglecting the region-to-region variations? If so, which average curve is the most appropriate, especially in low- A_V , high-latitude regions?

Perhaps the most standard dust map in use is the composite COBE-IRAS (Cosmic Background Explorer-Infrared Astronomical Satellite) map developed by Schlegel et al. (1998). These authors constructed a map of dust column densities from a combination of maps of dust emission at different far-IR wavelengths and made corrections using an H_I map. The dust columns were then converted into reddening $(A_B - A_V)$ using a calibration sample of ~ 400 elliptical galaxies whose intrinsic B-V colors were inferred from the dust-insensitive Mg₂ spectroscopic index (Faber et al. 1989). It should be pointed out that in the case of a curve varying across the sky, the Schlegel et al. (1998) map may more closely follow extinction at 1 μ m than $A_B - A_V$ (Schlafly et al. 2010). This may explain the temperature-related local departures in the Schlegel et al. (1998) reddening map with respect to $A_B - A_V$ determined independently using a statistical method (Peek & Graves 2010). Furthermore, Schlafly & Finkbeiner (2011) used another statistical method to derive reddening maps in SDSS areas, finding an overall normalization different by 14% from Schlegel et al. (1998). Reddening maps were expanded in coverage to 3/4 of the sky by using colors of Pan-STARRS1 (Panoramic Survey Telescope & Rapid Response System) stars (Schlafly et al. 2014) and providing finer resolution compared to the Schlegel et al. (1998) map. Another high-resolution reddening map was produced using H_I data by Lenz et al. (2017), but covering 40% of the sky.

Schlafly et al. (2010) found the optical slope of the extinction curve to vary across the highlatitude sky (2.7 < R_V < 3.4, i.e., 1.29 < A_B/A_V < 1.37), but less than the traditional Galactic plane sightlines derived using the pair method, thus justifying the use of a universal extinction curve. Berry et al. (2012) found a very similar range in slopes when combining optical and NIR constraints. Interestingly, a similarly small range of variation in R_V ($\sigma = 0.2$) was found along the Galactic plane (Schlafly et al. 2016), where the reddening is typically ten times higher than at high latitudes. Furthermore, Schlafly et al. (2016) find that optical slopes are correlated with the dust emissivity, though the origin of the correlation remains unknown.

Schlafly et al. (2010) and Schlafly & Finkbeiner (2011) found that the Fitzpatrick (1999) extinction curve with $R_V = 3.1$ slope agrees better with their optical constraints than either the CCM curve or its update by O'Donnell (1994) (with any R_V). However, at longer wavelengths, Schlafly et al. (2016) find that the Fitzpatrick & Massa (2009) NIR curve is a better choice than any other literature parameterization, presumably because of its R_V -dependent shape (**Figure 4d**). When it comes to the UV, obtaining an accurate high-latitude extinction curve is more difficult owing to the presence of the bump and shallower data from the GALEX satellite. Yuan et al. (2013) found that the FUV extinction is 2/3 of near-UV extinction, in contrast to standard extinction laws,

which predict similar extinction in the two bandpasses. In contrast, using colors of galaxies, Peek & Schiminovich (2013) found that FUV and near-UV extinction are as much as 50% and 25% higher, respectively, than the Fitzpatrick (1999) extinction, which would make the high-latitude Galactic extinction curve more similar to the LMC 30 Dor curve and therefore not part of the MW single-parameter family. This finding supports the idea that the UV-optical slopes of extinction curves may care more about the column density than in which galaxy they are measured.

Reddening maps continue to improve as well as does our understanding of the variation of the extinction curve across the sky. Extinction curves agree well with the standard curves in the optical range, but more work is needed to understand the departures in the UV at high Galactic latitudes.

4. THE THEORY OF DUST EXTINCTION LAWS

In this section, we synthesize broader trends in the theory of interstellar extinction and modeling efforts. For a comprehensive review of the relevant equations, we point the reader to the excellent Saas-Fee notes by Draine (2004).

4.1. Extinction Law Theory: Basic Framework

The optical depth seen by photons interacting with dust is $\tau_{\rm dust}(\lambda) = N_{\rm d} Q_{\rm ext}(\lambda) \pi a^2$, where $N_{\rm d}$ is the column density of dust, a is the size of the grain (therefore assuming a spherical geometry) and $Q_{\rm ext}$ is the ratio of the extinction cross section to the geometric cross section. The extinction cross section is the sum of the absorption and scattering cross sections, and it depends on the grain composition (Draine 2011). In order to develop a theoretical model for the extinction law, one must therefore simultaneously develop a model for the size distribution (a) as well as for the composition of the interstellar grains.

Most theories are constrained by a variety of observed emission and absorption features associated with dust. The existence of the 2175-Å extinction bump (e.g., Stecher & Donn 1965) points to at least some carbonaceous grains in the ISM (owing to corresponding absorption features in sp^2 -bonded carbon sheets; Draine 2011). This connection is amplified by extinction features at \sim 3.4 μ m that are likely due to carbon-based grains (e.g., Duley & Williams 1983). At the same time, absorption and emission near 9.7 μ m and 18 μ m indicate the likely existence of silicates as an important constituent of interstellar dust (e.g., Gillett et al. 1975, Kemper et al. 2004). These constraints have motivated two major types of modeling efforts: synthesis models and direct numerical simulation. In what follows, we summarize progress in each area.

4.2. Extinction Law Theory: Synthesis Models

The essence of synthesis modeling is the development of a theory that simultaneously models the grain size distribution and dust composition while remaining constrained by (a) the observed wavelength-dependent extinction in the ISM, (b) polarization as a function of wavelength, (c) atomic depletion patterns in the ISM, and (d) the IR emission properties of galaxies. One of the first synthesis models, and indeed the quintessential study in this category, was performed by Mathis et al. (1977) (hereafter MRN), who utilized a nonparametric size distribution and solved for the best-fit grain size distribution. These authors found that a power-law size distribution of spherical grains of graphite–silicate composition (see also Hoyle & Wickramasinghe 1969) provided a reasonable model for the observed extinction law at the time.

The MRN model was extended by Draine & Lee (1984), in both wavelength coverage and the optical properties of the graphites and silicates. Further updates into the X-ray regime (i.e.,

extended dielectric functions for graphites, silicates, and silicon carbides) were developed by Laor & Draine (1993). Subsequent models have departed from the power-law grain size distribution. For example, Kim et al. (1994) utilized a maximum entropy method for deriving the size distribution. Similarly, Li & Draine (2001) characterized the size distribution of very small grains by multiple log-normal distribution functions.

The past few decades have seen significant updates to the graphite-silicate model for dust. The first major class of models were extensions that included a PAH component (e.g., Siebenmorgen & Kruegel 1992, Dwek et al. 1997, Li & Draine 2001, Weingartner & Draine 2001, Siebenmorgen et al. 2014); these studies typically describe PAHs as carbonaceous grains, with the mass fraction divided into PAHs versus graphites as a free parameter. Generally, in these models the small PAH molecules contain <10³ C atoms and have physical and chemical properties similar to those of larger graphite-like grains, though in reality there are some significant differences arising from the C-H bonds in PAHs. Weingartner & Draine (2001) derived a size distribution of grains to match observed extinction patterns in the Galaxy, LMC, and SMC, and included PAHs such that \sim 15% of the interstellar C abundance was locked up in PAHs. A significant step forward was taken by Draine & Li (2007), who leveraged the results from the Spitzer Space Telescope to derive a size distribution of PAHs that reproduces the average MW emission spectrum (though note that the absorption cross section of PAHs remains a significant uncertainty; e.g., Siebenmorgen et al. 2014). Other models in the graphite-silicate family include amorphous carbons or composite particles consisting of a mixture of silicates, refractory organic materials, and water ice (e.g., Zubko et al. 2004, Galliano et al. 2011), and models with silicates with organic refractory mantles combined with very small carbonaceous particles and possibly PAHs (e.g., Desert et al. 1990, Li & Greenberg 1997).

These models largely treat interstellar dust as a mixture of different constituents, meaning that while the 2175-Å carrier drives FUV extinction, often a separate species is also included to contribute to the FUV extinction when the 2175-Å bump is not present. An alternative class of models, monikered the core-mantle models, sought to unify these populations by treating dust grains as a silicate core with a carbonaceous mantle that varies in composition or depth depending on the environment (e.g., Greenberg 1986, Duley 1987, Jones et al. 1990, Li & Greenberg 1997, Ysard et al. 2016). Recently, Jones et al. (2017) have developed the THEMIS framework, which provides a model for a core-mantle grain that varies in composition and/or mantle depth based on the response to the local environment (e.g., volumetric/surface densities, radiation field).

4.3. Extinction Law Theory: Numerical Models

In recent years, computational advances have permitted the direct simulation of the evolution of dust grains (in aggregate) in galaxy evolution simulations, which serves as a complement to synthesis models in understanding extinction in galaxies. The relevant physical processes governing the total dust mass are formation in stellar ejecta, growth by accretion of gas-phase metals, and destruction by sputtering in hot gas, whereas the grain-size distribution is primarily governed by shattering and coagulation processes. In practice the processes are actually linked, as growth rates may depend on the surface area of the grain (Kuo & Hirashita 2012). Of course, the problem must be initialized: A grain size distribution from different production processes (i.e., supernovae or AGB stars) is typically assumed as a boundary condition.

A significant step forward in the numerical modeling of the evolution of grain sizes was made by Asano et al. (2013) and Nozawa et al. (2015), who aggregated the relevant equations for the aforementioned processes and embedded them in a simplified (one-zone) galaxy evolution model, demonstrating the feasibility of a self-consistent galactic chemical evolution model wherein the size distribution of grains could be directly simulated. These models were extended by

Hirashita (2015), who developed a two-size approximation as a means for reducing the computational load of dynamically modeling a broad size spectrum of dust grains in bona fide hydrodynamic galaxy evolution simulations. Here, grains are divided into large (typically $a > 0.03 \mu m$) and small ($a < 0.03 \mu m$) grains. This model has been adopted by a number of groups since then (e.g., Aoyama et al. 2018, Gjergo et al. 2018, Hou et al. 2019) and has been shown in at least some cases to reproduce the results from multigrain models when the large and small grains represent log-normal distributions (Hirashita 2015).

Multiple grain sizes have been implemented in idealized hydrodynamic galaxy evolution simulations (Aoyama et al. 2018, McKinnon et al. 2018). By combining these size distributions with assumed extinction efficiencies from the literature, Aoyama et al. (2018), McKinnon et al. (2018), and Hou et al. (2019) extended their numerical simulations of extinction curves in galaxies. These groups find the physics of coagulation and shattering to be critical in reproducing both the FUV rise and 2175-Å bump in MW-like extinction curves.

The current galaxy-formation simulations include either single-size grains (e.g., McKinnon et al. 2016, Zhukovska et al. 2016, Popping et al. 2017b, Davé et al. 2019, Li et al. 2019, Vijayan et al. 2019) or two grain sizes (e.g., Hirashita 2015) into cosmological galaxy-formation simulations, or they include multiple grain sizes into idealized simulations (e.g., Asano et al. 2013, McKinnon et al. 2018). In the next few years, we anticipate numerical models to progress significantly through the implementation of a full size distribution of grains in cosmological hydrodynamic simulations on the fly to develop cosmological models for the grain size evolution in galaxies as they evolve across cosmic time.

5. ATTENUATION CURVES: THEORY AND MODELING

We now turn our attention from extinction to attenuation and begin by providing an overview of the status of theoretical models aimed at understanding variations in the shapes of attenuation laws. We first outline the landscape of different methods, which vary in spatial scale from the regions surrounding individual star clusters to cosmological volumes. We then aggregate the key results that thread through different models, attempting to synthesize major themes that have emerged over the past few decades in this area.

5.1. Basic Concepts

Fundamentally, all models deriving attenuation laws share the same basic methodology: (a) They develop a model for the structure of galaxies and populate them with stars and ISM; (b) they make assumptions regarding the extinction properties of the dust grains in those galaxies; and (c) they model the radiative transfer of stellar light as it escapes these systems. The major difference between models lies in how the star-dust geometry is specified. Simulation methods range from relatively simplified analytic prescriptions for galaxy structure to complex hydrodynamic galaxy-formation simulations. More complex simulations likely reflect a more realistic star-dust geometry, though at the expense of both increased computation time and ease in isolating the impact of individual physical phenomena on the final dust attenuation curve.

Analytic models were pioneered by Witt & Gordon (1996, 2000) and have been employed by a number of groups in subsequent years (e.g., Gordon et al. 1997, Charlot & Fall 2000, Pierini et al. 2004, Inoue 2005, Fischera & Dopita 2011). These models were expanded upon by Seon & Draine (2016), who developed a model for a 3D turbulent ISM patch within a galaxy, described by a clumpy geometry and a log-normal gas density distribution function. Other groups have developed analytic models for the one-dimensional radial structure of dust in galaxies in efforts

to model the dust attenuation curve (e.g., Inoue et al. 2006, Popescu et al. 2011). The structure of the ISM in analytic models can range from simple screen models (e.g., Calzetti et al. 2000) to models that include stellar birth clouds (e.g., Charlot & Fall 2000, Wild et al. 2011a).

Increasing in complexity, a number of groups have turned to semianalytic models (SAMs) in order to derive the attenuation properties of a diverse population of galaxies (e.g., Granato et al. 2000, Fontanot et al. 2009, Fontanot & Somerville 2011, Wilkins et al. 2012, Gonzalez-Perez et al. 2013, Popping et al. 2017a). In the context of galaxy-formation simulations, SAMs are a family of models that draw on a combination of either analytic or numerical models for halo growth over cosmic time, with analytic prescriptions for the evolution of the baryonic content and structure within halos (see the overview by Somerville & Davé 2015). The majority of SAMs employ a relatively simplified galaxy structure (for example, a stellar bulge embedded in an axisymmetric disk of gas, dust, and stars). Although the geometry of galaxies in SAMs is still analytically prespecified, SAMs build on the complexity of the aforementioned static models in that the stellar population content (i.e., age and radial distribution) are cosmologically motivated.

Hydrodynamic galaxy evolution models offer increased sophistication in their computed stardust geometries, though this costs computation cycles. The highest-resolution hydrodynamic models are idealized galaxy simulations that take place not in a cosmological context but rather by evolving galaxies that are initialized with a simplified geometry (e.g., Jonsson et al. 2006, Rocha et al. 2008, Natale et al. 2015). In hydrodynamic models, the star-dust geometry can vary over time owing to secular dynamical processes, as well as the redistribution of gas and dust due to stellar/AGN (active galactic nucleus) winds, though the effects of cosmic accretion and structural changes that are due to hierarchical merging will be missed. These issues are mitigated by large-box cosmological simulations (or cosmological zoom-in simulations), which model individual galaxies in their native cosmic environment (e.g., Narayanan et al. 2018a, Trayford et al. 2020).

5.2. Theoretical Drivers of Attenuation Law Slope Variation

A general source of consensus among theoretical models of attenuation laws is the role of the stardust geometry in galaxies as well as the impact of dust column density. The former are broadly subdivided into two regimes: geometry on the scale of birth clouds surrounding star clusters, and the large-scale geometry of diffuse dust in the ISM. We do not discuss the global geometry (i.e., viewing angle), as this is simply a manifestation of the aforementioned effects.

5.2.1. The role of birth clouds. Fanelli et al. (1988) found that the attenuation toward nebular lines in their sample of galaxies was significantly higher than that of the stellar continuum. The result was confirmed by Calzetti et al. (1994), who found the typical ratio of $A_B - A_V$ reddening to be \sim 2. These results motivated the introduction of a two-component (or age-selective) model of dust attenuation by Charlot & Fall (2000). In their model, the radiation from all stars is subject to attenuation by a diffuse dust (ISM) component, but stars below a threshold age $t_{\text{threshold}}$, corresponding physically to the dispersal time of the birth cloud (\sim 10 Myr; Blitz & Shu 1980), see an additional source of attenuation by way of a natal birth cloud.

The Charlot & Fall (2000) model assumes that birth clouds and the ISM each attenuate light according to fixed power-law attenuation curves, which we refer to as the component curves, to distinguish them from the resulting effective attenuation curves:

$$A_{\lambda} = \begin{cases} A_{V, \text{ISM}} \left(\frac{\lambda}{\lambda_{V}}\right)^{-n_{\text{ISM}}} + A_{V, \text{BC}} \left(\frac{\lambda}{\lambda_{V}}\right)^{-n_{\text{BC}}} & t \leq t_{\text{threshold}} \\ A_{V, \text{ISM}} \left(\frac{\lambda}{\lambda_{V}}\right)^{-n_{\text{ISM}}} & t > t_{\text{threshold}} \end{cases},$$
 11.

where n_{BC} and n_{ISM} correspond to power-law exponents for the diffuse ISM and natal birth clouds. Charlot & Fall (2000) found that a single power-law exponent ($n_{\text{ISM}} = n_{\text{BC}} = 0.7$), though with different normalizations for the optical depths of birth clouds ($A_{V, \text{BC}}$) and diffuse dust ($A_{V, \text{ISM}}$), was able to sufficiently satisfy both the nebular line constraints and the Meurer et al. (1999) relationship between the IRX and the UV slope (IRX $-\beta$) in nearby galaxies (see Section 8.1.2 for more details). The slope of the birth cloud curve was later argued to be $n_{\text{BC}} = 1.3$ by da Cunha et al. (2008), and this value is used in the SED fitting package MAGPHYS.

The effective attenuation curve resulting from the Charlot & Fall (2000) model evolves with time (becoming steeper) following a strong burst of star formation. Furthermore, Inoue (2005) showed that because young luminous stars suffer from extra attenuation and also dominate at short wavelengths, the resulting effective curve will be steeper than the component curves. In the Inoue (2005) analytical model, the effect of the clumpy geometry on the attenuation curve arises primarily because high-density regions contain young luminous stars.

The two-component model has shown significant utility in the nearly two decades since its publication. For example, Trayford et al. (2020) showed that hydrodynamic galaxy-formation models require the inclusion of a birth cloud component to match the observed optical depth-attenuation curve slope relation in galaxies (discussed further in Section 5.2.2). Similarly, the birth cloud model has allowed for additional degrees of freedom in SED fitting software, including both age-selective attenuation and the ability to model birth clouds with a range of parameterized curves, and not just the power-law curves as in the original model (e.g., CIGALE; Noll et al. 2009a).

5.2.2. The relationship between geometry and the slope of the attenuation law. Theoretical models are largely in consensus about the relationship between the geometry of the star-dust mixture in galaxies and the slope of the dust attenuation law. In short, more simplified geometries with obscuration in the UV result in steeper curves, whereas more complex geometries with clumpy dust result in flatter curves.

This result was first demonstrated in the seminal series by Witt & Gordon (1996), Gordon et al. (1997), and Witt & Gordon (2000), who used simplified analytic geometries to highlight the impact of the star-dust geometry on the slope of the attenuation curve. These authors found that, as a general rule, as the inhomogeneity increased in the ISM structure, attenuation curves become grayer (flatter). This result has been amplified in the literature by both analytic models (e.g., Ferrara et al. 1999, Bianchi et al. 2000, Charlot & Fall 2000, Inoue 2005, Fischera & Dopita 2011, Wild et al. 2011a) and hydrodynamic or similar methods (Natale et al. 2015; Seon & Draine 2016; Trayford et al. 2017, 2020; Narayanan et al. 2018a). The general physical driver behind grayer attenuation curves with more complex star-dust geometries is that UV photons from massive stars more easily escape and reduce the net measured optical depths at short wavelengths. Narayanan et al. (2018a) showed that a similar effect can transpire for normalized attenuation curves with increasing fractions of unobscured old stars as well, underscoring the concept that more complex geometries generally result in grayer curves.

5.2.3. The relationship between dust content and the slope of the attenuation law. Another important driver of the attenuation curve slope is the total dust column density along the line of sight. As observed by (e.g.) Salmon et al. (2016) and Salim et al. (2018), larger optical depths A_V correspond to grayer (shallower) attenuation curves. Many theoretical studies have predicted this effect (Witt & Gordon 2000, Pierini et al. 2004, Inoue 2005), but it was in particular highlighted by Chevallard et al. (2013), who aggregated and analyzed a diverse series of theoretical attenuation law studies by Pierini et al. (2004), Tuffs et al. (2004), Silva et al. (1998), and Jonsson et al. (2006) and showed that all the studies predict, with some normalization differences, a relationship

between the optical depth, A_V , and attenuation law slope. This relationship was subsequently postdicted in hydrodynamic cosmological zoom simulations (Narayanan et al. 2018a), as well as in large-box cosmological hydrodynamic simulations (Trayford et al. 2020). A physical origin for the optical depth–slope relationship was posited by Chevallard et al. (2013). Although the scattering albedo used by most theoretical studies is roughly constant in the optical, the phase functions are not: Red light scatters more isotropically than blue. Red photons emitted in the equatorial plane of the galaxy are more likely to escape, whereas blue photons have a comparatively increased likelihood of remaining and, subsequently, being absorbed. In the low optical depth limit, this corresponds to a steepening of the attenuation curve. In the high A_V limit, the contribution to the UV is dominated by stars located outside the $\tau=1$ surface, and the shape of the curve is flattened by both scattering into the line of sight and radiation from unobscured OB stars (Narayanan et al. 2018a).

5.3. The Origin of 2175-Å Bump Variations in Attenuation Curves

When simulating bump strength variations in attenuation curves, theoretical models differ fundamentally on one central point: Is it possible to create a bump-free attenuation curve when the underlying extinction curve has a bump in it? Posed another way, does the 2175-Å bump strength in the attenuation curve tell us anything about the intrinsic bump strength in the extinction curve?

The first class of models requires either removing the bump from the underlying extinction curve or significantly reducing it in order to produce a bump-free attenuation curve. For example, early models by Gordon et al. (1997) and Witt & Gordon (2000) that employed simplified analytic geometries found that a silicate-dominant grain composition (i.e., SMC-like dust) that does not have a bump was necessary to produce bump-free attenuation curves. Similarly, Fischera & Dopita (2011) found, using turbulent slab models, that destroying the 2175-Å carriers in the underlying extinction curve is the most efficient means of producing a bump-free curve. More recent high-resolution models of a turbulent ISM by Seon & Draine (2016) have found that radiative transfer effects can work to reduce the bump strength in galaxies, though a reduced bump amplitude (by \sim 60–70%) in the underlying Weingartner & Draine (2001) dust model is necessary to produce fully bump-free curves.

At the same time, a number of recent works have suggested that even galaxies whose dust properties allow for a bump can exhibit bump-free attenuation curves, owing to either the particulars of the star-dust geometry or albedo effects (e.g., Seon & Draine 2016). This is in contrast to studies that require a bump-free extinction curve to produce a bump-free attenuation curve. For example, Narayanan et al. (2018a) used a combination of dust radiative transfer calculations with cosmological zoom-in simulations of galaxy evolution to demonstrate that geometry effects alone can remove the bump from a galaxy's attenuation curve, even when using a traditional Weingartner & Draine (2001) size distribution and a Draine & Li (2007) composition (i.e., one that includes a bump). In this situation, UV emission from unobscured massive stars fills in the bump absorption feature. Similarly, Granato et al. (2000) and Panuzzo et al. (2007) utilized SAMs to show that a complex star-dust geometry can also fill in the UV bump, though, in contrast to Narayanan et al. (2018a), they also found that it was unobscured old stars providing the extra UV emission, as the massive stars by construction were obscured by birth clouds.

A strong constraint on models for bump variations was introduced by Kriek & Conroy (2013), who found that steeper attenuation curves for high-redshift galaxies have stronger bumps (Section 8.2). Seon & Draine (2016) and Narayanan et al. (2018a) found that radiative transfer effects and clumpier media tend to flatten attenuation curves as well as reduce bump strengths. In this class of models, then, a relationship between the bump strength and tilt of the curve is

natural. Unfortunately, models that employ reduced bump strengths in the underlying extinction curve and those that do not are able to match the Kriek & Conroy (2013) observed bump-tilt relation, thus limiting its utility in distinguishing between models.

5.4. Theory of the IRX- β Relation

The dust attenuation properties in galaxies are often characterized in terms of the relationship between their IRX and UV continuum slopes (β). The IRX is defined as

$$IRX \equiv \frac{L_{IR}}{L_{FUV}},$$
12.

where $L_{\rm IR}$ is the total IR luminosity, whereas the FUV luminosity is usually defined through the GALEX FUV filter or as monochromatic luminosity at 1500 Å or 1600 Å. The UV continuum slope, β , is defined as the index in the power-law relationship, $f_{\lambda} \propto \lambda^{\beta}$, over the wavelengths that lie in the 1200–3000-Å range (we discuss the observational methodology in Section 6.3). A relationship between the two for a fixed attenuation curve is natural: As UV energy is transferred into the IR through dust reprocessing, the UV power-law index, β , should redden. Furthermore, because the intrinsic, dust-free UV slope varies very little for star-forming galaxies with realistic star-formation histories and metallicities (Leitherer et al. 1999, Calzetti 2001), IRX- β can be used to probe the shape of the attenuation curve. This concept is demonstrated in **Figure 5**, where

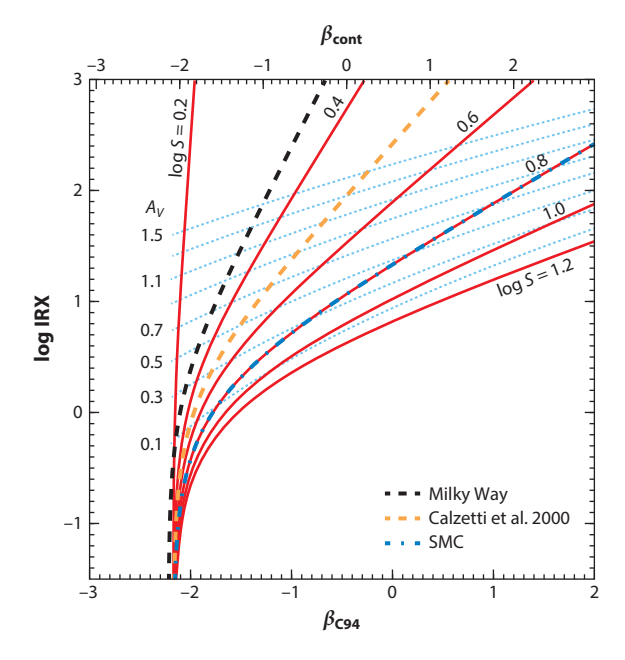


Figure 5

The IRX $-\beta$ diagram showing the loci of galaxies with different attenuation curve slopes S (including MW and SMC extinction and the Calzetti attenuation curves) and effective optical attenuations A_V . Curves are obtained from stellar population synthesis models attenuated using a Noll et al. (2009a) parameterization and restricted to the parameter space occupied by actual star-forming galaxies. The scatter in the IRX $-\beta$ plane at fixed attenuation is primarily the result of the varying attenuation curves of galaxies. The UV slope is defined using the Calzetti et al. (1994) windows and also converted to a continuous window value on the alternative axis. Abbreviations: IRX, IR excess; MW, Milky Way; SMC, Small Magellanic Cloud.

the loci of galaxies with different attenuation curve slopes (attenuated using the Noll et al. 2009a parameterization; Section 7) are shown alongside the MW and SMC extinction curves and the Calzetti et al. (2000) attenuation curve.

A wide range of theoretical methodologies have been employed to understand expectations for the observed IRX- β relation in galaxies. These include analytic models (Ferrara et al. 2017, Popping et al. 2017b), SAMs (e.g., Granato et al. 2000), idealized galaxy evolution simulations (Safarzadeh et al. 2017), and cosmological hydrodynamic galaxy-formation simulations (Mancini et al. 2016, Cullen et al. 2017, Narayanan et al. 2018b). For the most part, there is consensus among the varied theoretical efforts. Granato et al. (2000) demonstrated the importance of decoupled sites of emission of UV and IR radiation via consideration of the impact of birth cloud clearing times on their simulations. Similarly, Narayanan et al. (2018b) explicitly calculated the UV optical depths for hydrodynamic simulations of galaxy evolution to arrive at a similar point, whereas Popping et al. (2017b) cast this result in the context of holes in obscuring dust screens, as well as the impact of increased turbulence in the obscuring ISM. In short, increasing optical depths move galaxies along the IRX- β relation (**Figure 5**) while increasingly decoupled star-dust geometries (i.e., a proxy for varying attenuation curves) displace galaxies vertically in IRX $-\beta$ space. It is a point of consensus among theoretical models that the scatter in where star-forming galaxies present in IRX- β space is due to the diversity of underlying attenuation laws; this cause for the scatter has also been suggested in the interpretation of various observational data sets (e.g., Boquien et al. 2009, 2012; Mao et al. 2014; Álvarez-Márquez et al. 2019; Salim & Boquien 2019). What is unknown, however, is the root cause of the attenuation law variations. There is a degeneracy between variations in dust extinction curves (i.e., variations in grain sizes and/or the optical properties of grains) and the star-dust geometry in driving attenuation law variations. Both can impact the location of galaxies in the IRX- β space by modifying the attenuation curve.

5.5. Modeling Predictions

We now briefly show, by example, the relationship between extinction and attenuation in theoretical simulations by creating a plot (**Figure 6**) analogous to **Figure 4**, i.e., relating the slopes of attenuation curves to one another. It is evident that even though extinction curves along a number of sightlines in the Galaxy occupy a relatively narrow swath in these slope—slope and slope—opacity spaces, attenuation curves that use MW-like extinction curves underpinning the grain physics produce significantly more scatter, owing entirely to the complexities of the star-dust geometry and varying dust column densities.

For this exercise, we utilize the cosmological hydrodynamic MUFASA simulations presented by Narayanan et al. (2018a), which were run in a (25 Mpc)³ box with 512³ particles. These were coupled with stellar population synthesis (SPS) models and 3D dust radiative transfer simulations (Narayanan et al. 2015) that determine the attenuation of the stellar radiation. The models presented here include galaxies at z = 0 and z = 2. The input extinction curve in the simulation is fixed at the MW curve given by Weingartner & Draine (2001) and shown in **Figure 6a**. The Calzetti et al. (2000) attenuation and SMC extinction curves are shown for reference, along with median curves (medians of A_{λ}/A_{V} at each λ) from the simulations, binned according to different optical opacities. **Figure 6b** shows simulation predictions for the relationship between the UV and optical slopes. The plot extends to much steeper UV and optical slopes than the equivalent plot for the extinction curves (**Figure 4b**). There is a correlation between the UV and optical slopes in a sense similar to the trend seen in individual extinction sightlines in the Galaxy, though it is roughly two times wider than the extinction relation. This is a consequence of the star-dust geometry giving a wide range of attenuation laws, even for fixed grain size distribution and composition.

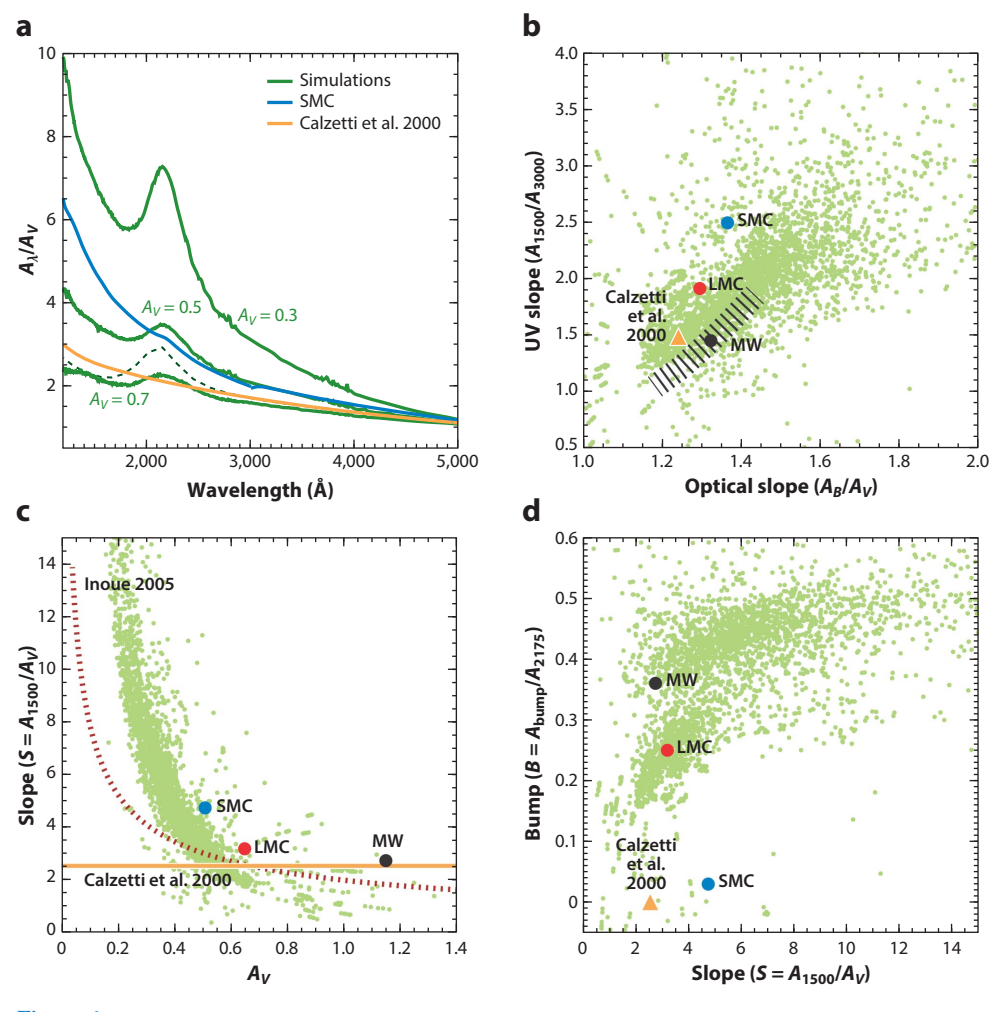


Figure 6

Predicted attenuation curves from hydrodynamic cosmological simulations coupled with radiative transfer modeling. (a) Median simulated curves in several bins of optical opacity, alongside the Calzetti et al. (2000) and SMC curves as comparisons. The dashed line represents the input extinction curve (of the MW) used in simulations. (b) The UV versus optical slopes, indicating that there is a correlation, though much wider than the single-parameter family of MW extinction curves (black stripes). (c) A very strong correlation of the UV-optical slope on optical attenuation, also predicted using analytical models of Inoue (2005) (dotted line). (d) Correlation of the UV bump strength with the UV-optical slope. Abbreviations: LMC, Large Magellanic Cloud; MW, Milky Way; SMC, Small Magellanic Cloud.

Moving to the overall UV-optical slope ($S = A_{1500}/A_V$), which is easier to constrain observationally than the UV or optical slope alone, we show its relationship with the optical opacity in **Figure 6c**. The simulations help to elucidate a trend such that more opaque galaxies have shallow curves. Specifically, galaxies with $A_V > 0.6$ are expected to have slopes shallower than the Calzetti curve. Remarkably, galaxies with $A_V < 0.4$ are expected to have steeper curves than even the SMC. The slopes change exponentially, with the highest values corresponding to the power-law index of 2.0. A scatter around the trend is ~ 0.12 in $\log S$. We also show the results (assuming the SMC

extinction curve) of the analytical two-component model of Inoue (2005), which employs a fixed clumpy geometry wherein young stars are only found in dense clumps. A higher fraction of young stars in dense regions may be responsible for a shift toward lower A_V . Finally, as pointed out in Section 3, the mean extinction curves for the MW, LMC, and SMC appear to follow a qualitatively similar trend between the slope of the curve and the mean opacity of sightlines.

In **Figure 6***d*, we turn our focus to the relationship between the predicted bump strength and the slope of the attenuation curve. The bump strength is correlated with the slope, which may reveal the impact of star-dust geometry on bump strength in that the reduced bump strength appears to correspond to decreased UV opacity, which is consistent with the explanation provided earlier in this section.

6. METHODS OF OBSERVATIONALLY DERIVING DUST ATTENUATION CURVES

Broadly, in order to derive the attenuation curve for a galaxy, one must be able to infer the unattenuated SED. The methods for deriving the dust attenuation curve can be divided into two categories based on whether this unattenuated (or less attenuated) galaxy SED is inferred empirically or is established based on the SPS models. Methods can also be characterized based on whether they derive attenuation curves for ensembles of galaxies in aggregate or aim to do so for individual galaxies.

6.1. Empirical Comparison Methods

For the empirical methods, it is important to classify or rank galaxies by attenuation in order to use less attenuated galaxies as references. Ideally, the comparison galaxies should be without dust and have the same intrinsic SED as dusty galaxies, but in practice the dust content of comparison galaxies can be nonzero so long as their (relative) attenuation can be accurately determined.

Calzetti et al. (1994) pioneered work on attenuation curves with the introduction of a template empirical method, which they applied to derive the attenuation curve of local starburst galaxies. The method first produced a relative attenuation curve $(A_{\lambda} - A_{V})$, which was then anchored with the IR data (Calzetti et al. 2000) to get the absolute curve (A_{λ}/A_{V}) . The data, consisting of UV– optical spectra, were binned into six groups, based on the value of their Balmer decrements. The Balmer decrement measures the attenuation of HII regions surrounding massive stars and is used in this method as a proxy for the stellar continuum attenuation on the basis of its correlation with the steepness of the UV slope (β) , which for continuously star-forming galaxies will mostly vary as a result of dust attenuation and, less so, due to the variations in mean population age or stellar metallicities (Calzetti et al. 1994). The spectra in each group of galaxies are averaged (after normalizing by the flux at 5500 Å) to produce template spectra. The template based on the galaxies with the smallest Balmer decrement is then used as a reference spectrum, to which other templates are compared to obtain relative attenuation curves $(\delta A_{\lambda} - \delta A_{V})$. These curves are normalized by the relative attenuation between the templates from the Balmer decrement, converted to stellar attenuation using a fixed factor, and then averaged to obtain the final relative attenuation curve. The method of Calzetti has been adapted by Battisti et al. (2016) to use UV photometry instead of spectra.

Attenuation at some wavelength is required to go from a relative attenuation curve to an absolute attenuation curve. As in the case of an extinction curve, this anchoring can be accomplished by assuming that attenuation approaches zero at longer wavelengths (Calzetti 1997, Battisti et al. 2017a), but the result depends on the exact method of extrapolating to infinite wavelength (Reddy et al. 2015). In the case of attenuation curves, anchoring can also be achieved using dust emission,

by requiring that the luminosity absorbed by the dust in stellar continuum match the luminosity emitted by the dust, i.e., the total IR luminosity (Calzetti et al. 2000). In principle, the template method can be adapted to use the IRX instead of the Balmer decrement. In that case, the absolute attenuation curve (A_{λ}/A_{V}) can, in principle, be determined without separate anchoring. An IRX-based empirical method is used by Johnson et al. (2007), who compare colors of galaxies of similar age but different IRX to derive aggregate attenuation curves.

A variant of the template method is the pair method of Kinney et al. (1994), in which individual galaxies are compared instead of the templates. In this method, the galaxies are assumed to be intrinsically similar, but with different effective dust attenuations. Wild et al. (2011a) adapted this method to large samples in the SDSS and constructed attenuation curves by averaging a large number of pair comparisons, in each of which one member is significantly more attenuated than the other as judged by their Balmer decrements. The galaxies in the pair are chosen to have similar redshifts, specific SFRs, metallicities, and inclinations. Observed SEDs are anchored in the *K*-band, where the attenuation is relatively small, so no separate anchoring is needed as in the case of Calzetti et al. (1994). Importantly, in the pair method the Balmer decrements are not used explicitly to derive attenuation but only to determine which galaxy is more attenuated.

In certain fortuitous cases in which two galaxies overlap, the attenuation curve of a foreground galaxy (its overlapping part) can be obtained using an empirical method originally developed by White & Keel (1992), in which the background galaxy serves as the backlight with SED known from the nonoverlapping portion (e.g., Berlind et al. 1997, Elmegreen et al. 2001, Holwerda et al. 2009, Keel et al. 2014). A similar method can be used to derive the attenuation curves of resolved dust lanes in early-type galaxies (Viaene et al. 2017b).

The principal advantage of empirical methods is that they do not require a parameterization, allowing the shapes of the curves or their features to be studied in greater detail, especially with spectroscopic data (e.g., Noll et al. 2007, 2009b). Template-based empirical methods do not derive the slopes of attenuation curves of individual galaxies. Their main disadvantage is the implicit assumption that individual curves are relatively homogeneous and on average similar between different templates or between the members of a pair. If that is not the case and, in particular, if the slope of the curve depends on the dust content itself, the curves characteristic of the dustier template/pair member will carry a greater weight in the final average curve (Wild et al. 2011a). More generally, if individual curves span a large range of slopes, then there is no single attenuation measure that allows ranking (e.g., $A_{1500, 1} > A_{1500, 2}$ does not imply $A_{V, 1} > A_{V, 2}$).

6.2. Model-Based Comparison Methods

Theory predicts that attenuation curves should vary dramatically from galaxy to galaxy (e.g., Narayanan et al. 2018a; Section 5.2). To quote Conroy (2013, pg. 407), "the use of a single dust attenuation curve for analyzing a wide range of SED types is [...] without theoretical justification." Nevertheless, for a long time SED fitting techniques were performed with fixed attenuation curves. A fixed-curve approach is implemented partially because of computational ease (allowing a well-sampled free curve increases the computation time significantly), and also because of the perceived futility of constraining the attenuation curve due to the well-known dust-age-metallicity degeneracy. Recently, however, it has been shown that useful constraints on the curve are possible even without IR data (Kriek & Conroy 2013, Salim et al. 2016, Salmon et al. 2016). As a result, the SED fitting technique is gaining momentum as a method for the determination of attenuation curves.

Currently two popular SED fitting packages, CIGALE (Boquien et al. 2019) and PROSPECTOR (Leja et al. 2017, Johnson et al. 2019), allow attenuation curves to be derived in a parametric form. SED fitting techniques involve the employment of SPS models in the creation of a library, or grid,

of dust-free galaxy SEDs, spanning a range of star-formation histories and stellar metallicities (given a fixed stellar initial mass function, isochrones, and atmosphere models). These SEDs are then attenuated according to some dust prescription to yield observed SEDs, from which the model observed-frame photometry is extracted. The fitting is performed next, in which observed photometry is compared with model photometry with known galaxy parameters (the mass-to-light ratio, specific SFR, ages, attenuation, etc.). SED fitting techniques for galaxies were traditionally used to identify a single best-fitting model, whose galaxy parameters were then adopted as the nominal values (e.g., Spinrad & Taylor 1971, Faber 1972, Sawicki & Yee 1998, Papovich et al. 2001). The assessment of errors in the best-fitting approach could be achieved by refitting with perturbed input photometry (e.g., Wiklind et al. 2008). Subsequently, Bayesian fitting techniques have been developed (Kauffmann et al. 2003; Salim et al. 2005, 2007; Noll et al. 2009a; Leja et al. 2017; Johnson et al. 2019) in which posterior probability distribution functions (PDFs) for every galaxy parameter of interest (or their combination) are derived. Adopting the mean or the median of a PDF as the nominal value results in more robust estimates than a single most-likely model, and the width of a PDF provides an estimate of parameter errors.

Significant improvements in the estimation of A_{λ} using the SED fitting method emerge if constraints from dust emission are included (Burgarella et al. 2005). SED fitting techniques that include IR photometry are typically referred to as energy-balance methods, because the IR SED is normalized in models in such a way that the total IR luminosity from stellar-heated dust emission matches the luminosity absorbed by the dust in UV through NIR. In energy-balance SED fitting, the shape of the IR SED is described by parameters that, depending on the IR model, range from a single parameter (Dale & Helou 2002) to six parameters (da Cunha et al. 2008). The addition of parameters increases model library sizes and fitting computation time if the entire SED is fit concurrently. However, unless the stellar continuum properties are tied to the shape of the IR SED (e.g., through the specific star-formation rate; da Cunha et al. 2008), the IR SED fitting is essentially decoupled from the UV through NIR SED fitting. This has led to an alternative approach, SED+L_{IR} fitting, in which the IR luminosity is determined separately, and then used as a direct energy-balance constraint in the UV-NIR SED fitting (Salim et al. 2018). Furthermore, in cases in which there is only a single reliable flux point, or the IR SED is not well-sampled in the far-IR, the latter approach allows the IR luminosity to be reasonably well determined from luminosity-dependent IR templates (e.g., Chary & Elbaz 2001) and then used in the SED+ $L_{\rm IR}$ fitting.

Using SED fitting to constrain the dust attenuation curve or other galaxy properties is a powerful technique if employed appropriately. First, the model colors must cover the parameter space of observed colors. If that is not the case, the ranges of model quantities (the priors) need to be expanded or adjusted. Ensuring a good match typically requires the inclusion of emission lines in the models or their exclusion from broadband photometry (Kauffmann et al. 2003, Salim et al. 2016). If a match cannot be achieved, it is best to exclude the bands that cannot be properly modeled because they may bias the fits of good bands. Similarly, the systematic photometry errors need to be chosen adequately to yield the expected best-fit χ^2 distribution of the ensemble, as well as the expected distribution of individual photometry band residuals.

The dust attenuation curve in the SED fitting can be implemented directly as an effective curve or using the Charlot & Fall (2000) two-component model (see Section 5.2.1). Note that the attenuation curve pertaining to birth clouds is very poorly constrained by SED fitting (e.g., Conroy et al. 2010, Lo Faro et al. 2017), so it is justified to keep it fixed or to tie it to the slope of the ISM dust attenuation curve. In the latter case, the resulting effective curve is different (steeper) than the input (component) curves because younger populations that dominate at shorter wavelengths suffer higher attenuation (Inoue 2005).

An additional uncertainly can arise when modeling objects that may include an AGN. Specifically, when including the IR data, care must be taken to exclude the contribution of AGN heating to the IR luminosity, which can be significant in IR selected samples at higher redshift (Daddi et al. 2007). If the IR SED is well sampled, the AGN contribution can potentially be mitigated by including it in the modeling (e.g., Leja et al. 2018).

Finally, we note that although the modeling approach for deriving attenuation curves has mostly been employed using SED fitting techniques, there are some exceptions. Conroy et al. (2010) use models to predict UV and optical colors and compare them with aggregate colors of galaxy with different inclinations. Scoville et al. (2015) identify a sample of intrinsically similar galaxies with ongoing SF (as evidenced by Civ absorption) and young mean ages (a small Balmer break), for which they derive an average attenuation curve by comparing the SEDs with model (dust-free) starburst spectra. Conroy (2010) observes the change in colors of galaxies as a function of redshift and compares it with model predictions to constrain the UV bump strength as it traverses the observed wavelengths. Finally, some studies derive an attenuation curve as a part of detailed modeling of a galaxy SED using radiative transfer calculations (e.g., De Looze et al. 2014).

6.3. The IRX- β Method

The IRX $-\beta$ method can be considered an offshoot of model-based methods, having specifics that justify separate treatment. The IRX $-\beta$ diagram relates the IRX to the power-law exponent β of the observed UV SED slope (Meurer et al. 1995; Section 5.4). For star-forming galaxies, IRX is tightly correlated with $A_{\rm FUV}$ or A_{1500} . Meurer et al. (1999) showed that local starburst galaxies (overlapping with the sample of Calzetti et al. 1994) occupy a relatively narrow locus in the diagram, forming an IRX $-\beta$ relation. The potential existence of a relation was significant because it laid the foundation for a straightforward correction of UV emission in galaxies where IR observations are lacking, based on the easily observable UV slope (or color).

The observed UV slopes of star-forming galaxies range from $\beta = -2.5$ to $\beta = 2$. However, the SPS models predict the intrinsic (dust-free) UV slopes to span a range that is 10 times smaller, $-2.5 < \beta_0 < -2.1$, even when galaxies with extremely high specific star-formation rates (sSFRs) in the early Universe are considered (Cullen et al. 2017). Consequently, an IRX- β diagram with a dust-corrected x axis would look like a narrow pillar of points. To more clearly illustrate the point, let us assume that the horizontal width of the pillar in IRX- β space is zero. Reddening these points with a fixed attenuation curve shifts them to the right in a way that preserves the zero width. This is because a given IRX in combination with a fixed curve can yield only a unique value for the observed β (or UV color). Therefore, in the case of a small spread of intrinsic UV colors, the scatter in the observed IRX- β plane must result from a diversity of attenuation curves in the UV. Steep IRX- β slopes would correspond to shallow attenuation curves and vice versa. We show this explicitly in **Figure 5**.

For a given attenuation curve parameterization (Section 7) and assumed bump strength, one can therefore construct a mapping between the values of IRX and β , on one hand, and the values of attenuation curve slope and A_V on the other. Following Salim & Boquien (2019), one can parameterize the IRX- β plane in a way that directly translates to the slope of the attenuation curve:

$$\log S = a_0 \frac{\beta - \beta_{\min}}{\log(\text{IRX/BC} + 1)} + a_1.$$
13.

We use minimization of scatter of low-redshift galaxies from Salim & Boquien (2019) to find $\beta_{min} = -2.17$ and BC =1.65, in excellent agreement with the Overzier et al. (2011) values for local starbursts. The parameters assume that the UV slope β is determined over 10 spectral windows,

following Calzetti et al. (1994). Other definitions can yield significantly different values of β . For example, the slope obtained from fitting over the entire SED continuum from 1268 to 2580 Å (β_{cont}) is related to β from Calzetti et al. as $\beta_{\text{cont}} = 0.55 + 1.21\beta_{\text{C94}}$ (Salim & Boquien 2019). The mapping between the slope of the attenuation curve and IRX- β is subject to some degree of degeneracy because the UV bump can affect β (Mao et al. 2014), modifying the coefficients in Equation 13 and introducing noise. The degeneracy can be alleviated using the fact that the bump strength and the UV slope in real galaxies are to some degree correlated (Kriek & Conroy 2013). Therefore, using the above sample of low-redshift galaxies and assuming that attenuation curves follow the modified Calzetti curve parameterization (Section 7), we obtain $a_0 = 0.42$ and $a_1 = 0.08$. The slope S is recovered with a root-mean-square of 0.08 dex. The intrinsic UV slope shifts toward the blue as a function of the specific SFR relatively slowly $[d\beta_0/(d \log \text{sSFR}) = -0.13]$, suggesting that Equation 13 with locally determined coefficients and a small shift in β_{min} would be applicable at higher redshifts. For a given attenuation curve parameterization, A_V can also be derived from the IRX- β diagram, as shown by the tracks in Figure 5.

The scatter in the IRX $-\beta$ plane can thus be used to probe the diversity of attenuation curve slopes. This connection has been explicitly exploited in a number of studies (e.g., Salmon et al. 2016, Cullen et al. 2017, Lo Faro et al. 2017, McLure et al. 2018, Reddy et al. 2018, Álvarez-Márquez et al. 2019), and implicitly in many more. However, in practice, the IRX $-\beta$ method has several issues. First, it is difficult to measure the UV slope without being affected by the 2175-Å UV bump (e.g., Buat et al. 2011, Tress et al. 2018). Even if the bump is removed or accounted for, the estimate of β will depend on the choice and width of filters, the redshift, and the wavelength range over which the slope is fit. Furthermore, though the effect is smaller in comparison with that of the UV bump degeneracy, the intrinsic UV slope (which is dependent on the choice of isochrones and atmosphere models) will depend on the sSFR (or mean age), potentially complicating comparisons at different redshifts (Reddy et al. 2018). Finally, the IRX $-\beta$ plane directly probes the UV part of attenuation curves (Lo Faro et al. 2017).

7. PARAMETERIZATIONS OF ATTENUATION CURVES

Ideally, one wishes to determine an effective attenuation curve spanning a range from the Lyman continuum to the NIR, and with sufficient spectral resolution to reveal any small-scale features. This is not possible with broadband photometric data. Furthermore, when using the SED fitting method, it is necessary to describe the attenuation curve with a small number of parameters, which gives rise to various proposed parameterizations.

Many common parameterizations consist of a single parameter related to the overall slope of the curve, and, optionally, one or more parameters specifying the UV bump. The first two parameterizations discussed here were originally developed to describe extinction curves in the Galaxy, but they can in principle also serve as parameterizations for attenuation curves.

We start our discussion with the CCM (Cardelli et al. 1989) parameterization of MW extinction curves introduced in Section 3. The detailed shape of these curves is specified by four dozen parameters (coefficients), of which one, the optical slope (R_V), is allowed to vary. In the CCM parameterization the UV bump is not adjustable, but this can be achieved with appropriate modifications (Conroy et al. 2010). As far as we know, the CCM parameterization is not currently implemented in any publicly available SED fitting code but has been used in some studies (e.g., Hagen et al. 2017).

Another single-family parameterization originally derived for MW extinction curves is that by Fitzpatrick (1999), which extends to the optical and NIR a very flexible parameterization developed by Fitzpatrick & Massa (1988) for spectroscopic extinction curves in the UV. In its full form

this parameterization contains four parameters related to the overall shape of the curve, but they can be made internally dependent so that only R_V is allowed to vary, leading to a single family of curves. In addition, there are three parameters that specify the strength, the central wavelength, and the width of the UV bump based on a Drude profile (Fitzpatrick & Massa 1986).

Moving away from extinction curve parameterizations, Noll et al. (2009a) developed a parameterization in which they took the Calzetti et al. (2000) attenuation curve and allowed it to have a variable slope and a Drude function profile to describe the bump. The parameter used to produce a family of curve slopes is the power-law exponent δ , such that $\delta=0$ corresponds to the unmodified Calzetti curve, and $\delta<0$ produces curves that are steeper than it. The UV-optical slope of the curve S and δ are related as

$$\log S = 0.40 - 0.55 \,\delta. \tag{14}$$

The modified Calzetti curve parameterization is currently implemented in the SED fitting code CIGALE in a form described by Boquien et al. (2019) and Salim et al. (2018). It is also available in PROSPECTOR (Leja et al. 2017), but with the bump tied to the value of the slope according to a relation from Kriek & Conroy (2013).

All of the previous parameterizations produce curves whose shapes are based on empirical extinction or attenuation curves. A less nuanced approach is to describe the attenuation curve as pure power law, which also requires one parameter (*n*).

In **Figure 7**, we show the four aforementioned parameterizations in terms of the relationships between UV-optical slope and the optical slope (**Figure 7***a*), and just the UV slope against the

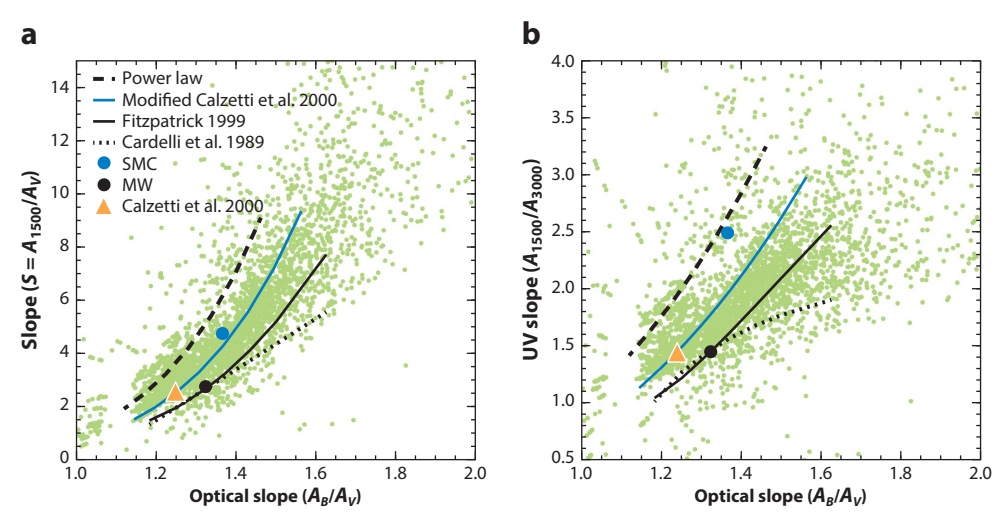


Figure 7

Tracks corresponding to four different one-parameter parameterizations overlaid on simulated attenuation curves from Narayanan et al. (2018a) that are based on the MW input extinction curve. Panel a shows the overall slope and panel b the bump strength against the optical slope. Power-law curves span 0.5 < n < 1.7, modified Calzetti curves span $-1.0 < \delta < 0.4$, and the Fitzpatrick (1999) and Cardelli et al. (1989) curves span $1.6 < R_V < 5.5$. Although it is not shown, modeling of dust attenuation using the two-component (age-selective) model, such that the curves are applied to young and old populations separately, will result in effective attenuation curves that are shifted (mostly along the tracks) and have some scatter. Positions occupied by MW and SMC extinction curves and the Calzetti et al. (2000) attenuation curve are shown for reference. Abbreviations: MW, Milky Way; SMC, Small Magellanic Cloud.

optical slope (**Figure 7***b*). For illustration purposes, we also show simulated attenuation curves from Narayanan et al. (2018a). Some parameterizations follow the simulations better than others, but with the important caveat that Narayanan et al. (2018a) assume a single extinction curve as an input (that of the MW), and true curves may fill the parameter space differently. The bottom line is that each of the four parameterizations covers a significantly different part of the parameter space and, being single-parameter curves, none can capture the diversity of the simulated curves. Some broadening of the loci (\sim 0.07 in A_B/A_V) can be accomplished when the curves are applied in a two-component fashion, i.e., with different normalization for young and old stars (Section 5.2.1.)

The simulations of Narayanan et al. (2018a) do not extend in the NIR to inform us about the performance of parameterizations in that regime, but if we use the MW extinction curves from Fitzpatrick & Massa (2009) as a guide, either the family of modified Calzetti curves or the power-law curves are likely to be more realistic than the CCM or Fitzpatrick & Massa (1990) parameterizations for no other reason than because the latter are essentially fixed curves in this wavelength range.

8. ATTENUATION CURVES: OBSERVATIONAL RESULTS

In previous sections, we built the theoretical foundation of extinction and attenuation laws, showed model results, and surveyed the landscape of methods for deriving attenuation curves. We now discuss the observational results relating to attenuation curves at low and high redshift.

In short, we aim to aggregate results regarding variations in the slopes ($S = A_{1500}/A_V$) and bump strengths ($B = A_{\rm bump}/A_{2175}$) in attenuation laws. For reference, the mean Galactic extinction curve has $S_{\rm MW} = 2.8$ and $B_{\rm MW} = 0.35$, whereas the mean SMC extinction curve has $S_{\rm SMC} = 4.8$ and $B_{\rm SMC} \approx 0$, based on the standard curves from Section 3. We refer to curves with S > 4 as steep.

We subdivide results based on two factors:

- 1. **Redshift:** We split the discussion into low redshift (z < 0.5) and higher redshift (z > 0.5), between which there is on average an order of magnitude difference in sSFRs and gas fractions, and a significant difference in the availability and sensitivity of the data.
- 2. **Method of deriving curves:** As we demonstrate, different methods often produce differing results with respect to the slopes and bump strengths, even for the same sample.

While reviewing the results, we keep in mind that the expected diversity in attenuation curves from theory (Section 6) implies that the results may differ even for the same redshift range and method, depending on sample selection.

8.1. Attenuation Curves of Galaxies at Redshifts Less Than Approximately 0.5

We first point the reader to **Figure 8**, where we summarize the slope (*S*) and bump strength (*B*) parameters obtained from several low-redshift studies. **Figure 8***b* highlights a large range of intrinsic (face-on) dust columns of galaxies ($0 < A_V < 0.6$) and how A_V is magnified by the viewing geometry.

8.1.1. Empirical methods. Calzetti et al. (1994, 2000) presented seminal work in deriving attenuation curves for nearby galaxies. Indeed, the mean curve derived from these studies has been a standard reference for more than two decades, and the Calzetti curve is a common assumption in the SED fitting models. The Calzetti et al. (1994) sample consisted of 36 starburst and blue compact dwarf galaxies with UV (from IUE) and optical spectra. The sample lies on average 1 dex above the local star-forming main sequence (the SFR– M_* relation), which has motivated the use

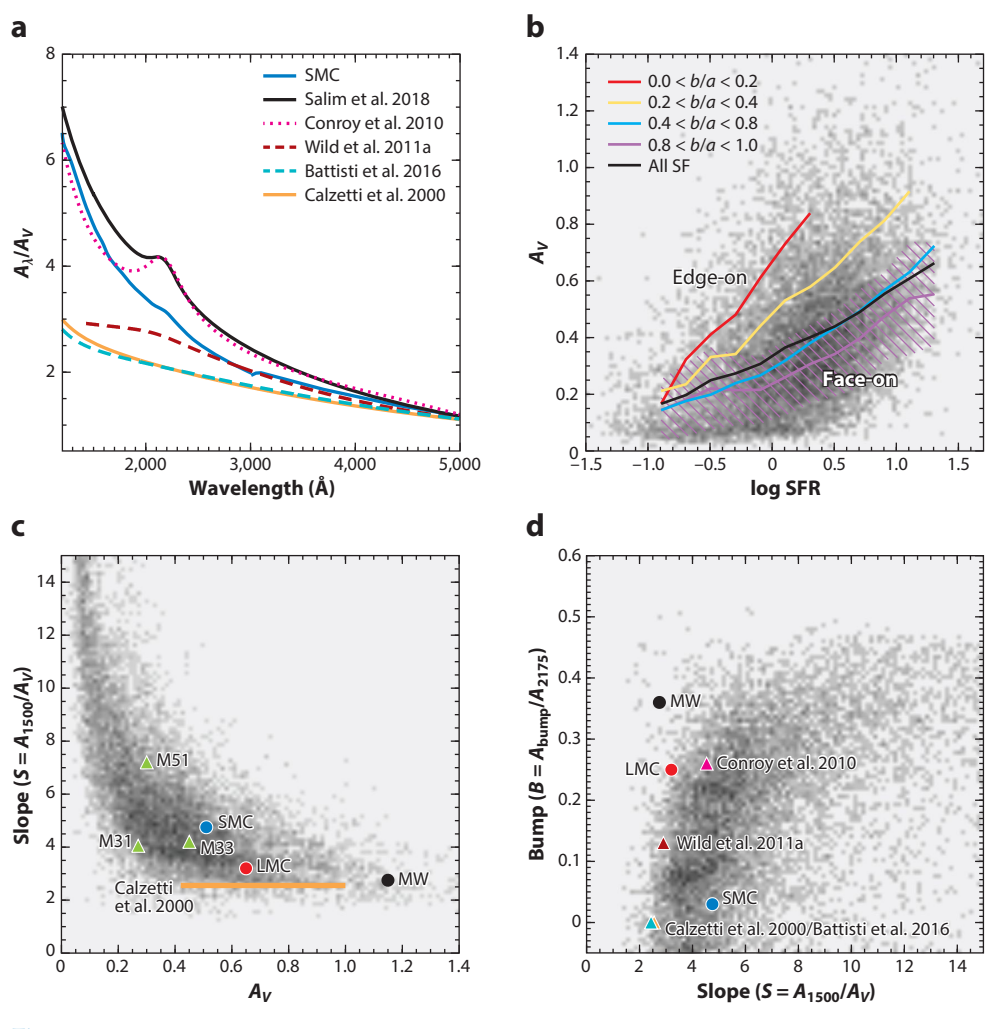


Figure 8

Observational characteristics of attenuation curves in the Local Universe. (a) The attenuation curves of Calzetti et al. (2000), Conroy et al. (2010), Wild et al. (2011a), Battisti et al. (2016), and Salim et al. (2018) in comparison with the average SMC extinction curve. The Wild et al. curve is given for disk morphology, b/a = 0.6 inclination and log sSFR = -10. The original Salim et al. curve has been rederived here based on deep UV photometry. (b) The change of optical depth of galaxies as a function of SFR and galaxy inclination. (c) The relationship between UV-optical slopes and A_V for individual galaxies. (d) The UV bump strength versus the slope. Underlying data for panels b-d come from GSWLC-D2 (Salim et al. 2018). The MW, LMC, and SMC represent mean extinction curves, whereas M31, M33, and M51 are attenuation curves from detailed radiative transfer modeling. Abbreviations: GSWLC, GALEX-SDSS-WISE Legacy Catalog Survey; LMC, Large Magellanic Cloud; MW, Milky Way; SF, star formation; SFR, star-formation rate; SMC, Small Magellanic Cloud; sSFR, specific star-formation rate.

of the resulting curve at high redshift, given the increased normalization of sSFR with redshift (e.g., Rodighiero et al. 2011, Madau & Dickinson 2014, Speagle et al. 2014). After anchoring the relative curve using IR luminosities (Section 6.1), the nominal Calzetti curve is relatively shallow (S = 2.6), similar to the slope of the MW extinction curve (**Figure 8a**), with a 1σ range on the

slopes of 2.3 < S < 2.9 (Calzetti et al. 2000). An important feature of the Calzetti curve is the significantly reduced (or nonexistent) 2175-Å UV bump. The absence of apparent bumps in the individual IUE UV spectra of 143 galaxies, which include some 20 normal star-forming galaxies and from which the Calzetti sample was drawn, was previously noted by Kinney et al. (1993).

The subsequent introduction of large surveys, in particular SDSS in the optical and GALEX in two UV bands, allowed the empirical study of attenuation curves to be extended to larger samples and to more normal star-forming galaxies. Similarly, the 2MASS and UKIDSS (UK Infrared Deep Sky Survey) surveys facilitated anchoring for curves by extending the measurements to the NIR. Battisti et al. (2016, 2017a) adapted the template method of Calzetti to use UV and NIR photometry and obtained aggregate curves of 5,500 galaxies with a 4000-Å break of <1.3 (corresponding to sSFR $< 10^{-10} \text{ year}^{-1}$), i.e., relatively young main sequence galaxies. Their average curve has essentially the same shallow slope (S = 2.4) as the Calzetti curve. Battisti et al. (2017a) also studied the average curves of subsamples as a function of stellar mass, sSFR, and gas metallicity but found no convincing trends, supporting the notion that the average attenuation curves of normal star-forming galaxies and starburst ones have similar slopes. Splitting the sample by inclination, Battisti et al. (2017b) did find a correlation with the attenuation curve slopes, in the sense that highly inclined galaxies have shallower slopes (S = 2.2) with a possible weak bump ($B \sim 0.1$), whereas face-on galaxies had steeper slopes (though still only S = 2.7). Battisti et al. (2016) tentatively concluded based on broadband UV colors and their relationship with the Balmer decrement that the UV bump was not seen in their sample. They later strengthened this conclusion based on a small sample for which GALEX UV spectra were available (Battisti et al. 2017b).

Other empirically based studies have obtained similar results. For example, the empirical method used by Johnson et al. (2007) finds relatively shallow (S > 2.5) slopes for 1,000 nearby galaxies split into several mass and 4000-Å-break bins, without obvious mass or age dependence. Wild et al. (2011a) use an empirical pair method (Section 6.1) to derive optical–NIR (and UV–NIR) curves for a sample of 23,000 (15,000) normal star-forming galaxies. They present results as a function of inclination, sSFR, and central stellar mass density. They find the NIR curve to be constant and the optical and UV curves to depend on inclination and morphology, though only weakly on the sSFR and optical depth. In particular, the strength of the UV bump was found to be stronger in edge-on galaxies. Overall, the UV–optical slope of various subsamples in their analysis varies in the range of 2.5 < S < 4.5 (i.e., mostly shallow), with a moderate bump ($B \sim 0.15$).

Overall, empirical studies find a possible diversity of attenuation curves, with trends depending on inclination but not (strongly) on sSFR (i.e., population age). On average, curves derived via empirical methods tend to be shallower than the SMC extinction curve. The evidence for UV bumps is mixed, but on average they do not seem to be as strong as the MW bump.

8.1.2. The IRX- β method. As demonstrated in Figure 5, the tight mapping between the position of a galaxy in the IRX- β plane and the shape of the attenuation curve allows one to deduce their properties (in particular its slope; Section 6.3). The original study of starburst galaxies with IUE found the IRX- β relation to be relatively narrow (Meurer et al. 1999). As UV observations with GALEX became available, galaxies with more normal SF were recognized to have a larger scatter compared with the Meurer sample and/or be offset from it (Buat et al. 2005, Seibert et al. 2005, Gil de Paz et al. 2007, Dale et al. 2009, Takeuchi et al. 2010). Several studies have subsequently rederived the Meurer relation using GALEX data (Overzier et al. 2011, Takeuchi et al. 2012, Casey et al. 2014b) and found it to be shifted downward, due to a factor of \sim 2 aperture losses in IUE UV photometry. This explanation for the offset was anticipated by Cortese et al. (2006), Gil de Paz et al. (2007), and Boissier et al. (2007). As pointed out by Seon & Draine (2016),

the new relations mostly eliminated the offset between starburst and normal galaxies, suggesting that the attenuation properties of starburst and star-forming galaxies are actually similar (i.e., their curve slopes).

A number of studies have investigated the source of scatter in the IRX- β relation of normal galaxies. Kong et al. (2004) attributed the dominant drivers of scatter to age-related parameters, such as the mean population age, sSFR, or birthrate parameter. This said, many subsequent works (e.g., Burgarella et al. 2005, Seibert et al. 2005, Johnson et al. 2007, Panuzzo et al. 2007, Boquien et al. 2009, Salim & Boquien 2019) did not find the age to be an important factor in driving the IRX- β scatter within the population of galaxies studied. The interpretation of these results would be that the slope of the attenuation curve is not strongly dependent on the age.

Moving away from regular starbursts and normal star-forming galaxies, numerous works have demonstrated that ultraluminous infrared galaxies (ULIRGs) tend to lie much bluer than the starburst relation (e.g., Goldader et al. 2002, Buat et al. 2005, Howell et al. 2010, Casey et al. 2014b), suggesting curves similar to or shallower than the Calzetti relation. Indeed, Casey et al. (2014b) found that galaxies with increasing IR luminosity at a given redshift have increasingly blue IRX $-\beta$ colors at both low and high redshift, a result subsequently postdicted by theoretical simulations (Safarzadeh et al. 2017, Narayanan et al. 2018a). The physical interpretation forwarded by Casey et al. (2014b), Safarzadeh et al. (2017), and Narayanan et al. (2018a) is that low optical depth sightlines toward unobscured OB associations drive bluer colors.

8.1.3. Model-based methods. Burgarella et al. (2005) presented a seminal study deriving attenuation curves from nearby galaxies via the SED fitting method. These authors analyzed 50 UV-selected and 100 IR-selected galaxies and, based on a single-population power-law parameterization that allows for a bump, found that individual galaxies span a range of slopes (2.5 < S < 6.2) and a range of bump strengths, from zero to almost MW-like. On average, their UV-selected sample had S = 4.5, which is almost as steep as the SMC, and a moderate bump (B = 0.2), i.e., half as strong as the MW bump. Conroy et al. (2010) applied a color-based method and two-component power-law model to a principal sample of 3,400 medium-mass (9.5 < $\log M_* < 10$) disk galaxies (Sérsic index < 2.5) to derive an average curve with the same steep slope (S = 4.5) as that of Burgarella et al. (2005), but a somewhat stronger bump of B = 0.26. More recently, as part of the demonstration of the Bayesian Markov Chain Monte Carlo SED fitting code PROSPECTOR, Leja et al. (2017) performed UV to mid-IR SED fitting on a diverse sample of 130 relatively massive galaxies and found a wide range of slopes in the 2 < S < 15 range. Using a larger sample, Salim et al. (2018) applied SED+L_{IR} fitting to obtain individual attenuation curves of 230,000 SDSS galaxies, including the galaxies below the main sequence. Curves were found to exhibit a very wide range of slopes (2 < S < 15), with the median slope S = 5.4, which is somewhat steeper than the SMC curve (**Figure 8***a*,*c*).

Both Leja et al. (2017) and Salim et al. (2018) find a strong relationship between the optical opacity and curve slope, such that the galaxies with higher A_V have shallower slopes. We show this relationship for individual galaxies in **Figure 8c**. Also shown are the slopes for M51, M31, and M33, determined from detailed 3D radiative transfer modeling (De Looze et al. 2014, Viaene et al. 2017a, Williams et al. 2019), which generally fall on the relation. Also shown are the slopes from standard extinction curves for the SMC, LMC, and MW. The MW point has high A_V because typical sightlines are in the Galactic plane.

The UV bump was also found to vary significantly in the curves derived by Salim et al. (2018), from no bump to values somewhat higher than the MW's bump, and with a median value of B = 0.2 (half the MW strength). These results support the existence of a correlation between the slope and the bump strength (**Figure 8***d*), which was previously found by Kriek & Conroy

(2013), in agreement with the simulations of Narayanan et al. (2018a) (**Figure 6**). The sense of the relation is that shallower slopes tend to have weaker bumps. Notably, it is the opposite of the trend in the SMC, LMC, and MW extinction curves and also differs from the Battisti et al. (2017b) attenuation curves, in which there are signatures of a bump only in the most inclined galaxies (those with shallower curves).

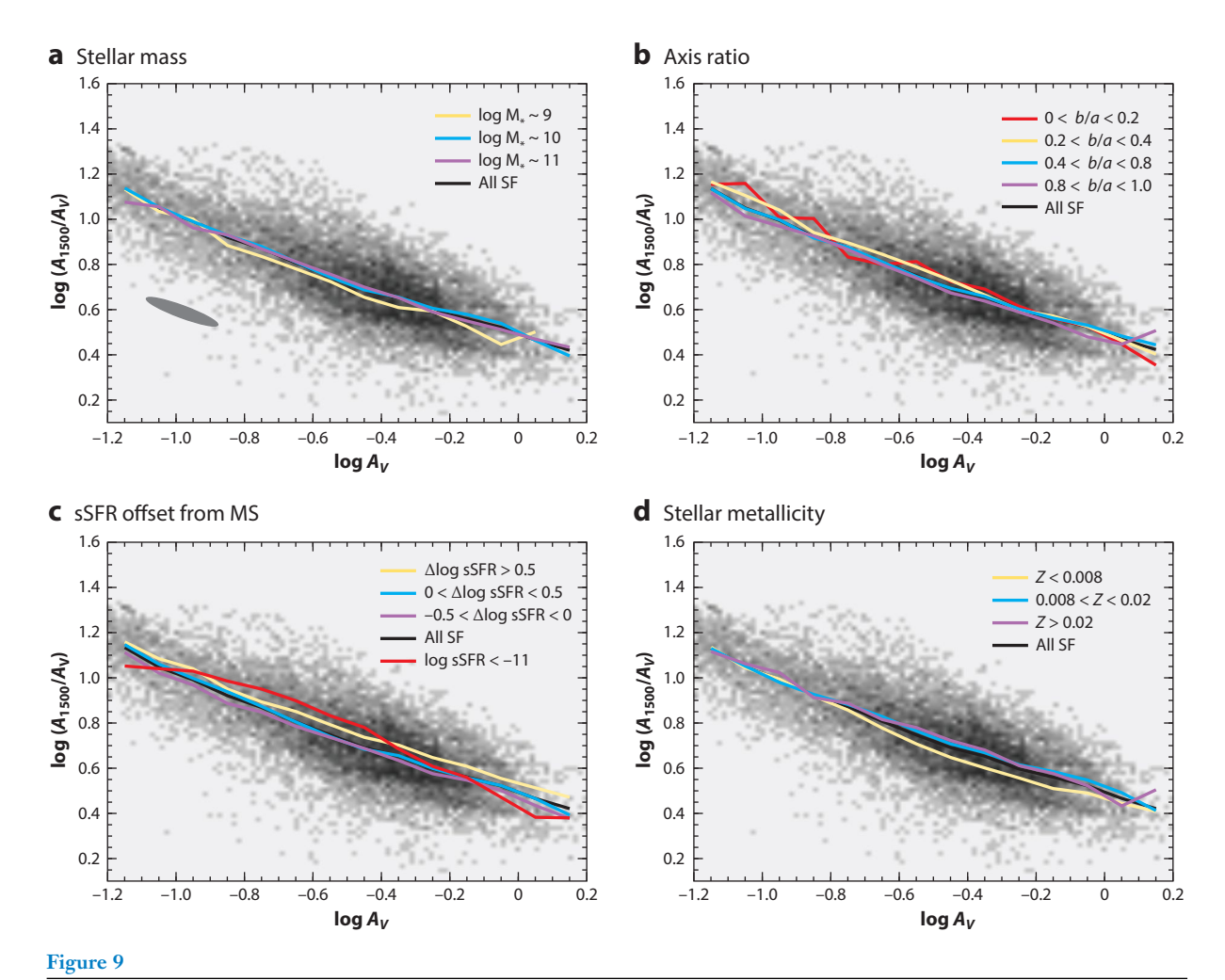
Recently, Decleir et al. (2019) has applied the SED+LIR method using UV photometry from the *Swift X-ray Telescope* in addition to GALEX to study the attenuation curve of the low-mass spiral galaxy NGC628 (M74) on global and resolved scales. The overall curve of this galaxy having average $A_V = 0.26$ is steep (S = 5.3), with a moderate bump (B = 0.14). Interestingly, individual regions also show slope versus A_V and slope versus bump strength relations. *Swift* photometry was found to significantly help constrain the curve, especially the UV bump.

As a method that yields attenuation curves for individual galaxies, the model-based studies have the potential of presenting us with the detailed demographics of dust properties and how they relate to other galaxy properties. Like empirical-method studies and IRX- β studies, the model-based studies find that there is no large difference in the average slopes of starburst and normal star-forming galaxies. Where model-based studies differ from empirical studies is that they find on average steeper slopes for similar samples of galaxies. There is tentatively also a discrepancy regarding the average strength of the bump: Model-based studies find moderate bumps (though not as strong as in the MW attenuation curve), whereas empirical studies find weak or no bumps. More work is needed to clarify these methodological and/or observational issues.

8.1.4. Drivers of the slope of attenuation curves in the Local Universe. Large samples of attenuation curves enable systematic investigations of the drivers of their diversity. Here, we use 23,000 galaxies with deep UV from GSWLC-2 [GALEX-SDSS-WISE (*Wide-Field Infrared Survey Explorer*) Legacy Catalog 2; Salim et al. 2018] and plot the slopes S versus A_V in **Figure 9**. First, we see that the slope- A_V relation has the power-law form,

$$\log S = \log(A_{1500}/A_V) = -0.680 \log A_V + 0.424.$$
 15.

The scatter around the relation is 0.12 dex, and most of it is intrinsic. This empirical relation is not as steep as the one predicted in modern cosmological simulations (cf. Figure 6c and Narayanan et al. 2018a), though it is qualitatively similar. The difference may arise from a higher fraction of young stars in dense regions in real galaxies (Inoue 2005). The principal question can be stated simply: What parameters other than the dust column density (for which A_V serves as a proxy here) may affect the shape of the attenuation curve, in particular its slope? The panels of Figure 9 show trend lines for subsamples of star-forming galaxies of differing (a) stellar mass, (b) inclination, (c) specific SFR with respect to the main sequence, and (d) stellar metallicity. The key point is that once A_V is fixed, none of the investigated factors has a significant effect on the slope of the attenuation curve. For example, more massive galaxies on average do have shallower curves, but this is because they have higher A_V ; i.e., they are shifted down the relation. Remarkably, the lack of difference in the slopes at fixed A_V is true even for galaxies with very different inclinations. A dusty galaxy with a face-on attenuation of A_V and a less dusty galaxy that has the same A_V (because we observe it edge on) will have the same attenuation curve slope, as predicted in the radiative transfer models analyzed by Chevallard et al. (2013). A similar situation exists for different levels of starformation activity: Galaxies from starbursts to green valley and quiescent galaxies below the main sequence (see **Figure 9**c) all have very similar slopes for a given A_V . A small trend may exist with respect to the metallicity (both stellar and gas-phase), such that more metal-rich galaxies have steeper slopes at fixed A_V , which may be a reflection of different dust grain properties rather than radiative transfer effects. Galaxies with different bump strengths (not shown) will have different



Dependence of the slopes of attenuation curves on galaxy physical parameters at $z \sim 0$. Log-log plots of the UV-optical slope versus A_V are based on the same data as that used in **Figure 8**. Each panel contains the same data and the same average trends for the full sample (black curves). Individual panels show trends for subsets of data binned by (a) stellar mass, (b) inclination (axis ratio), (c) sSFR offset from the MS (positive indicates above), and (d) the stellar metallicity. Except for the metallicity, none of the other factors affects the slope of the attenuation curve directly, but only by modifying A_V . The marginalized errors are ~ 0.1 dex in both coordinates and are highly correlated (ellipse in panel a). Abbreviations: MS, main sequence; SF, star formation; sSFR, specific star-formation rate.

slopes at a fixed A_V , in the sense that weaker bumps go with shallower curves. However, rather than being the driver of the dispersion, the trend either reflects the fact that low A_{1500} helps suppress the bump, as discussed in Section 5.3, or suggests that the bump and the dust composition are correlated (Weingartner & Draine 2001).

Residual intrinsic scatter of slopes at fixed A_V may be due to the differences in the intrinsic dust grain properties (i.e., the size distribution or composition), which are difficult to test. However, if the slopes of the extinction curves themselves follow A_V , as suggested in Sections 3.3 and 3.4, such that low A_V sightlines suffer steeper (SMC-like) extinction, we can speculate that the diversity of dust types at a given A_V may potentially be small.

We conclude that the dominant determinant in the slope of the attenuation curve, out of the considered physical parameters, is A_V . Galaxies with different inclinations, star-formation rates, and stellar masses to first order move up and down the more or less universal relation, depending on their A_V values.

8.2. Attenuation Curves of Galaxies at Redshifts Greater Than Approximately 0.5

Galaxies at high redshift differ in multiple ways from the present-epoch galaxies: At a fixed stellar mass they have larger gas fractions and star-formation rates, their morphologies and kinematics are less settled, and their gas-phase metallicities are lower (see the reviews, Shapley 2011 and Madau & Dickinson 2014). All of these factors may affect the dust content, properties of dust grains, and the resulting dust attenuation curves. The methodological and observational difficulties that affect the determination of average or individual attenuation curves at low redshift are exacerbated at higher redshifts due to smaller sample sizes, less sensitive or less complete photometry (especially in the IR), the reliance on photometric redshifts, more difficult identification of AGN contamination, and other related issues. Informed by low-redshift studies, we pay special attention to the properties of the samples being studied in order to account for the differences that may stem from the diversity of high-redshift populations. The general picture that is starting to emerge from studies of galaxies at high redshift is one that is in broad terms consistent with what is observed at low redshift: Galaxies exhibit a wide range of attenuation curve slopes, from gray, Calzetti-like curves to steeper than SMC curves.

Several high-redshift studies have found a correlation between the curve slopes and optical attenuation, similar to the results at low redshift. Potentially as a result of this relation, the IR-selected galaxies tend to exhibit shallower overall curves than UV or optically selected galaxies, with optically nearly opaque star-forming galaxies having the grayest curves. The UV bump is present at a variety of strengths and is on average correlated with the slope. **Figure 10** summarizes the results of a number of high-redshift studies.

8.2.1. Nebular versus stellar continuum attenuation. Before reviewing results related to attenuation curves, we highlight an important topic that has emerged in high-redshift studies: the quantification of the relative attenuation toward ionized regions versus the stellar continuum (reviewed in Steidel et al. 2014 and Shivaei et al. 2015). As found in the original Calzetti et al. (1994) study, evidence for increased attenuation toward nebular regions may indicate the presence of a birth cloud-like dust component (e.g., Charlot & Fall 2000). These results were confirmed for low-redshift galaxies in a large-scale study by Wild et al. (2011a). The results for the need for extra attenuation toward H_{II} regions at high z are mixed. Reddy & Steidel (2004), Erb et al. (2006), Reddy et al. (2012), and Shivaei et al. (2015) find that the reddening toward nebular regions is comparable with that of the stellar continuum when comparing X-ray, UV, $H\alpha$, IR, and radio-based star-formation rate indicators. At the same time, Förster Schreiber et al. (2009), Wuyts et al. (2011), Price et al. (2014), and Mieda et al. (2016) find the need for extra attenuation toward nebular regions, in agreement with the two-component birth cloud model. Förster Schreiber et al. (2009) made comparisons against some of the same galaxies as Erb et al. (2006) and suggested that aperture corrections may owe to the differing results regarding potential excess attenuation toward H_{II} regions. An important step forward was made by Price et al. (2014), who found not only the need for increased attenuation toward HII regions in their sample of \sim 150 $z\sim$ 1.5 galaxies drawn from the 3D-HST survey (Brammer et al. 2012) but also a decreased difference in $A_{\rm HII}$ compared to $A_{\rm UV}$ with increasing sSFR (also Puglisi et al. 2016). The physical interpretation is that for galaxies with very large sSFR, most of the stellar light is coming from

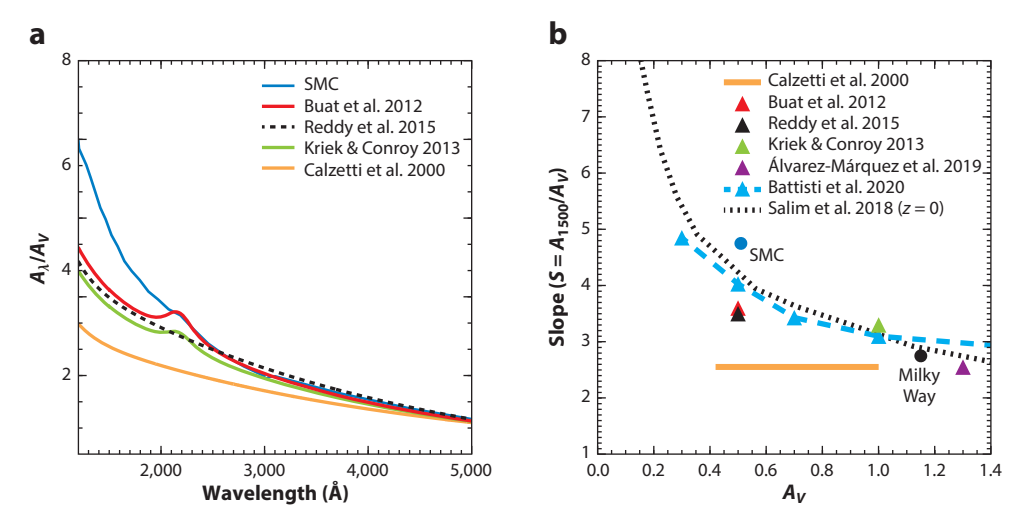


Figure 10

Observational characteristics of attenuation curves at z > 0.5. (a) Attenuation curves at z > 0.5 from Buat et al. (2012), Kriek & Conroy (2013), and Reddy et al. (2015) in comparison with the SMC and Calzetti et al. (2000) curves. The Buat et al. (2012) and Kriek & Conroy (2013) curves were constructed using the SED fitting method, whereas Reddy et al. (2015) use the empirical templates-based method. (b) The slope of curves compared with sample-averaged A_V . This panel adds data points for high-z galaxies split by A_V from Battisti et al. (2020) and the data point from Álvarez-Márquez et al. (2019). Abbreviations: SED, spectral energy distribution; SMC, Small Magellanic Cloud.

young stars that see both dust in HII regions and diffuse dust. In these situations, $A_{\rm HII} \approx A_{\rm UV}$. With decreasing sSFR, however, the contribution of older stellar populations to the integrated light outside of HII regions becomes important, and the relative difference in reddening between HII regions and the stellar continuum increases accordingly. A trend with sSFR indeed exists even at low redshift (Wild et al. 2011a), with the ratio of $A_B - A_V$ reddening for the nebular and the continuum reaching equality for extreme local starbursts (log sSFR ~ -8.7 ; Koyama et al. 2019).

Finally, we point out that the comparison of nebular and stellar continuum attenuation requires that the attenuation curves be known or correctly assumed for both components. Wild et al. (2011b) have found that the nebular attenuation curve has a slope similar to the MW extinction curve, rather than the SMC or the Calzetti curves, so the standard Galactic extinction law is recommended for correcting emission line fluxes.

8.2.2. Empirical methods. Studies using empirical methods (Section 6.1) have placed a number of constraints on the slopes of high-z attenuation curves. Early work by Reddy & Steidel (2004) found consistent results between X-ray- and radio-derived SFRs from UV-selected galaxies at 1.5 < z < 3, and those derived from dust-corrected UV photometry assuming a Calzetti et al. (1994) curve, implying a Calzetti-like curve is a reasonable descriptor of the attenuation in these galaxies. This result was confirmed by Shivaei et al. (2015), who used a similar method for a sample of \sim 250 z \sim 2 UV-selected galaxies.

Subsequently, a number of studies have found evidence for curves that depart from a Calzetti-like curve at high redshift. For example, using the spectroscopic data from the MOSDEF [MOSFIRE (Multi-Object Spectrometer for Infra-Red Exploration) Deep Evolution Field] rest-frame optical survey of 224 H-band selected $z\sim 2$ galaxies, Reddy et al. (2015) applied the Balmer-decrement-based template method of Calzetti et al. (1994) to derive relative attenuation

curves. These curves were anchored to absolute curves in several ways. Assuming zero attenuation at 2.9 μ m resulted in $R_V = 2.51$, which was adopted as the fiducial curve, and we show it in **Figure 10**. With the slope of S = 3.5, the curve sits roughly halfway in between the Calzetti (S = 2.6) and the SMC curves ($S_{\text{SMC}} = 4.8$) for a sample that has an average $A_V = 0.5$.

Reddy et al. (2015) find marginal evidence for the UV bump using broadband data, though the authors do not include it in their third-order polynomial attenuation curve fit. Noll et al. (2007) use a sample of 108 UV-selected galaxies, also at $z \sim 2$, assembled from several spectroscopic surveys. By looking at the difference in SED slopes shortward and longward of the bump peak, they find that galaxies on average have bump strengths close to that of the LMC 30 Dor extinction curve (B = 0.15) and essentially never as strong as the MW bump ($B_{\rm MW} = 0.35$). Similar results were obtained by Noll et al. (2009b) in a follow-up study of 78 galaxies in the same redshift range. In addition, they found that the width of the aggregate bump was 40% narrower than that in the MW. Conroy (2010) found that the broad–band colors of $z \sim 1$ galaxies are inconsistent with bumps as strong as the Galactic one if a shallow curve with MW-like slope is assumed. This said, a moderate bump in the Conroy (2010) sample is not excluded if the slope is steeper.

8.2.3. The IRX- β method. The principal challenge with the IRX- β method at higher redshifts lies in the fact that typical galaxy populations are too faint to be individually detected, especially at longer IR wavelengths. More recently, this limitation has been addressed by the application of stacking techniques and observations using Atacama Large Millimeter Array, and we primarily focus on those studies. Like low-redshift galaxies, galaxies at higher redshifts occupy a wide range of positions on the IRX- β diagram. Many studies find that high-redshift galaxies on average follow the original Meurer relation uncorrected for UV aperture losses (e.g., Siana et al. 2009, Bourne et al. 2017, Fudamoto et al. 2017, Koprowski et al. 2018, McLure et al. 2018, Wang et al. 2018). The interpretation of these results would be that, on average, these galaxies have attenuation curves similar to the Calzetti curve. Other studies find IRX- β relations that, when interpreted as attenuation curves, place them closer to the SMC curve (e.g., Heinis et al. 2013, Alvarez-Márquez et al. 2016, Pope et al. 2017, Reddy et al. 2018). Reddy et al. (2018) further find that lower-mass galaxies tend to have somewhat steeper attenuation curve slopes. The cause of the differing results is as yet not clear but could in principle arise from the differences in typical dust contents of the samples that have been selected in different ways. Furthermore, as pointed out in Section 6.3, the interpretation and comparison of the IRX- β results are made difficult by different methods of measuring the UV slope (e.g., Koprowski et al. 2018, Álvarez-Márquez et al. 2019) and the uncertainties in the magnitude of evolution of the intrinsic UV slope (Buat et al. 2012, Reddy et al. 2018).

In addition, there are notable deviations in how galaxies populate the IRX- β plane that go beyond the Calzetti-to-SMC range. They come in two general flavors: a cloud of galaxies that are particularly blue (i.e., low β), which lie above and to the left of the IRX- β relation corresponding to the Calzetti curve, and galaxies that have IRX values that place them below the SMC curve. Galaxies with blue UV spectral slopes are often selected as dusty star-forming galaxies (DSFGs; for a review, see Casey et al. 2014a) via a range of techniques (e.g., Penner et al. 2012, Oteo et al. 2013, Forrest et al. 2016). Casey et al. (2014b) demonstrated that galaxies with increasing IR luminosity have increasingly blue UV SEDs and speculated that this may be due to low-opacity sightlines toward UV-bright sources. This physical scenario corresponds to grayer attenuation curves driving galaxies upward in IRX- β space, as demonstrated explicitly in **Figure 5**.

An analogous situation going in the opposite direction may apply to galaxies detected at z > 5 that all appear to fall below the IRX- β curve associated with the average SMC attenuation curve (Capak et al. 2015, Bouwens et al. 2016, Barisic et al. 2017). Although the presence of these

high-redshift systems at very low IRX values may at least partially owe to an underestimate of the IR luminosity (e.g., Faisst et al. 2017, Narayanan et al. 2018b, Liang et al. 2019, Ma et al. 2019), some theoretical studies have found that the IRX $-\beta$ relation even for these low-metallicity systems is shaped predominantly by the attenuation curve itself (Narayanan et al. 2018b, Reddy et al. 2018, Ma et al. 2019) and would therefore indicate very steep curves.

Finally, we note recent interest in the IRX– M_* relation at high redshift (e.g., Bouwens et al. 2016, Álvarez-Márquez et al. 2016, Fudamoto et al. 2017). Locally, this relation has a scatter almost two times greater than the IRX– β relation (Salim & Boquien 2019), but when the stellar mass is added to the IRX– β relation as a three-dimensional plane showing the variation of IRX, β , and M_* for galaxies at a fixed redshift, it can help obtain more accurate predictions for IRX and reveal variations in the attenuation law across the stellar mass function at a given cosmic epoch.

8.2.4. Model-based methods. The application of SED fitting methods to derive attenuation curve parameters of high-redshift galaxies is a relatively recent method but has revealed important correlations in the attenuation curves of galaxies. Similarly, these techniques have elucidated the importance of the NIR portion of the attenuation curve in deriving physical properties of galaxies (Lo Faro et al. 2017).

Buat et al. (2011) performed UV through far-IR SED fitting of $30 z \sim 1.5$ galaxies selected at $160 \mu m$ with a Noll et al. (2009a) single-component parameterization. The average curve they found for these galaxies was shallow (S=3.0) and exhibited a moderate UV bump (B=0.17, 1/2 of $B_{\rm MW}$), without a correlation between the slope and the bump. This said, their IR selection resulted in a sample with a high average optical attenuation ($A_V=0.9$). Using similar techniques (with two-component dust modeling instead of one) and focusing on the same redshift range, but using a sample of 750 UV-selected galaxies of which about half are detected at $24 \mu m$, Buat et al. (2012) find a much greater diversity of attenuation curve slopes (2.7 < S < 6.3). The geometric average is S=3.6, which is very similar to the Reddy et al. (2015) curve (see **Figure 10**), with which it shares the average A_V of 0.5. In the Buat et al. (2012) study, the UV bumps take a wide range of strengths, rarely exceeding that of the MW, with an average of B=0.20. Buat et al. (2012) found no clear trend between the slopes of their attenuation curves and the bump strengths.

At the same time, Kriek & Conroy (2013) fit composite SEDs spanning from observed-frame optical to 8 μ m with the single-component Noll et al. (2009a) parameterization, constructed from galaxies at 0.5 < z < 2.0, and selected to have A_V > 0.5. Their binned curves span a range of slopes from Calzetti to the SMC, with an overall average of S = 3.3. The average bump strength is moderate, with B = 0.15 (**Figure 10**). An important result from the Kriek & Conroy (2013) study was a trend between the bump strength and the slope of aggregate curves, in the sense that the shallow (Calzetti-like) curves have smaller (but still detectable) bumps. In the same vein, Álvarez-Márquez et al. (2019) performed SED fitting on stacks of z ~ 3 galaxies binned by different properties and found slopes, on average, similar to the Calzetti one. Tress et al. (2018) performed SED fitting in the observed rest-frame optical to 3.6- μ m range of 1,800 galaxies at 1.5 < z < 3, exploiting 25 medium-band filters well placed to sample the UV bump. These authors found a strong correlation between bump strength and reddening, stronger than that with respect to the optical slope. The strength of UV bumps was found to occupy a similar range as in previous studies discussed in this section.

Most SED fitting studies find average slopes steeper than the Calzetti curve. In contrast, Scoville et al. (2015) used an alternative model-based method tailored for galaxies dominated by young stars and found a Calzetti-like slope. Their sample lies at 2 < z < 6, with an average $A_V = 0.6$. The average curve derived by Scoville et al. (2015) nevertheless shows some presence of a 2175-Å UV bump. Using a similar method, Zeimann et al. (2015) obtained, for a sample

of mostly lower-mass ($\log M_* < 10$) galaxies at $z \sim 2$, an aggregate curve agreeing with that of Scoville et al. (2015), except for a lack of the UV bump.

As discussed in Section 6, one expects a strong correlation between slope and A_V . Several studies have found this relation at higher redshifts, using attenuation curves derived from SED fitting techniques. For example, Arnouts et al. (2013) performed SED fitting with a two-component power-law dust model to 16,500 24- μ m-selected galaxies with z < 1.3. They found a very wide range of slopes (2.5 < S < 7.0), with the typical value of S = 4.2, and uncovered a correlation between the slope and the average optical opacity. Similarly, Salmon et al. (2016) performed SED fitting (without IR constraints) on $\sim 1,000$ individual galaxies at 1.5 < z < 3 detected at 24 µm. They too showed a diversity of attenuation curves, with similar average slopes as those of Kriek & Conroy (2013), and showed their slopes to be correlated with the reddening $(A_B - A_V)$. Recently, Battisti et al. (2020) performed energy-balance SED fitting of ~5,000 IR-detected galaxies (24 μm or longer) from the GAMA (Galaxy and Mass Assembly) and COSMOS (Cosmic Evolution Survey) surveys spanning 0.1 < z < 3. They present attenuation curves binned by A_V (excluding $A_V < 0.2$), which also show a correlation with the steepness of the slope. Their results for freeslope SED fitting, expressed as UV-optical slope S, are displayed in Figure 10b. Comparison with the low-redshift relation (Equation 15), based on Salim et al. (2018), suggests that the S-A_V relation may not evolve strongly with redshift. The UV bumps of Battisti et al. (2020), which are well constrained using medium-band data, are on average of moderate strength (B = 0.1) and not correlated with other galaxy parameters.

As in low-redshift studies, differing results at higher redshifts (especially from IRX $-\beta$ studies) are present, but some of the apparent discrepancies are alleviated with the consideration of the diversity of the samples, especially in terms of their dust content. Results may also depend on the methodology, and future studies should aim to resolve this question by applying several methods on the same sample and critically investigating these applications.

9. CONCLUSIONS

Large-scale panchromatic and spectroscopic surveys of galaxies, as well as large surveys of Galactic stars, have ushered in a new era in the empirical study of extinction and attenuation laws. Observational advances are further exploited by the development of new analysis and computational techniques, such as SPS coupled with Bayesian SED fitting or the use of standard crayons to study Galactic extinction. On the theoretical side, our understanding of dust grain physics is improving while radiative transfer modeling of attenuation in galaxies is becoming more sophisticated and placed in a larger context of galaxy evolution modeling.

We summarize the findings in this review article with some high-level conclusions regarding extinction and attenuation curves in galaxies.

- Local Group extinction curves show great diversity in slopes and UV bump strengths that may form a continuum of properties governed by grain size distribution and composition along with radiative transfer effects dependent on the dust column density. This continuum of properties is to be distinguished from a more simplistic discretized split into MW- or SMC-type dust.
- A great diversity of attenuation curve slopes (defined as the ratio of attenuation at short and long wavelengths) appears to be present in galaxies at low and high redshifts. For a given amount of optical attenuation, the FUV attenuation can be ~2–7× greater, corresponding to a range from shallower than the Calzetti curve to steeper than the SMC curve. Consequently, there is significant scatter between the optical and UV attenuations. This nonuniversality of attenuation curves is predicted by most radiative transfer models.

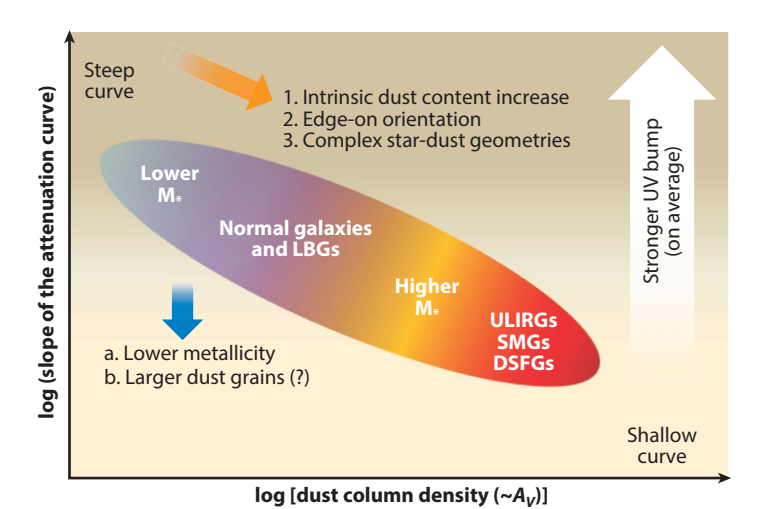


Figure 11

A schematic representation of the dependence of attenuation curve slope on dust column density (for which optical attenuation is a proxy), with possible drivers along the power-law relation (the *oval* and *orange arrow*) and possible factors driving the scatter (*blue arrow*). Abbreviations: DSFGs, dusty star-forming galaxies; LBGs, Lyman-break galaxies; SMGs, submillimeter galaxies; ULIRGs, ultraluminous infrared galaxies.

- Slopes correlate strongly with effective optical opacity, with opaque galaxies having shallower (grayer) curves. The dependence is probably a manifestation of a more fundamental dependence on the dust column density, for which the optical attenuation serves as a proxy. The dependence approximately follows a power law, and is schematically illustrated in Figure 11. Theoretical work informs us that the dependence may be the outcome of a combination of radiative transfer effects (scattering and absorption) and local geometry effects (clumpiness of dust). In the Local Universe, accounting for optical opacity largely removes residual trends in the slope with respect to the stellar mass, sSFR, or galaxy inclination.
- The 2175-Å UV bump feature also shows a great range in strengths, from effectively nonexistent to somewhat above the MW strength (with the bump strength defined as the fraction of attenuation at 2175 Å due to the bump). There is a correlation between the UV bump strength and the attenuation curve slope. Models that reproduce this correlation ascribe bump variations to the infilling from unobscured stars, but intrinsic dust composition differences may also play a part.
- The above diversity of curves means that the average curves of galaxies of different stellar masses or SFRs (whose dust contents differ) and of galaxies selected by dust emission (e.g., ULIRGs, DSFGs, submillimeter galaxies) will span a wide range as well.

FUTURE ISSUES

- 1. What drives the evolution of the grain size distribution in galaxies across the mass function over cosmic time?
- 2. Is there a more unifying framework that explains MW extinction curves alongside those that fall outside of the single-parameter family?

- 3. What is the minimum number of independent parameters necessary to develop a parameterization for attenuation curves that captures the diversity of effective attenuation curves across different spectral regimes?
- 4. We should improve the understanding of systematics affecting different observational methodologies in order to resolve the issues in which the same samples of galaxies can return different results for attenuation curves.
- 5. What are the potential drivers of attenuation curve slope differences beyond the optical opacity that can be probed observationally? How much of the scatter is due to the different intrinsic extinction curves? How do we test this?
- 6. What are the characteristics of attenuation curves in the Lyman continuum region?
- 7. Can we use the results from theoretical modeling to better inform SED fitting software (via, e.g., mapping theoretically derived attenuation curves to observations via learning algorithms)?

DISCLOSURE STATEMENT

The authors are not aware of any affiliations, memberships, funding, or financial holdings that might be perceived as affecting the objectivity of this review.

ACKNOWLEDGMENTS

The authors thank Andrew Battisti, Véronique Buat, Charlie Conroy, Akio Inoue, Ben Johnson, Mariska Kriek, Joel Leja, Naveen Reddy, Eddie Schlafly, David Schlegel, Kwang-Il Seon, Alice Shapley, Irene Shivaei, Sébastien Viaene, and Thomas Williams for helpful conversations, comments, or data. The authors thank Sidney Lower for her assistance in generating **Figure 2**, and Bobby Butler for technical assistance and proofreading. S.S. wishes to thank Janice C. Lee for inspiring discussions over the years, as well as past and current developers of CIGALE SED fitting code, in particular Médéric Boquien. D.N. wishes to express gratitude to Charlie Conroy and Karin Sandstrom for getting him interested in this field to begin with. D.N. was supported in part by National Science Foundation grant number AST-1715206 and *Hubble Space Telescope* grant number AR-15043.001.

LITERATURE CITED

Álvarez-Márquez J, Burgarella D, Buat V, et al. 2019. Astron. Astrophys. 630:A153

Álvarez-Márquez J, Burgarella D, Heinis S, et al. 2016. Astron. Astrophys. 587:A122

Aoyama S, Hou K-C, Hirashita H, Nagamine K, Shimizu I. 2018. MNRAS 478:4905–21

Arnouts S, Le Floc'h E, Chevallard J, et al. 2013. Astron. Astrophys. 558:A67

Asano RS, Takeuchi TT, Hirashita H, Nozawa T. 2013. MNRAS 432:637-52

Barisic I, Faisst AL, Capak PL, et al. 2017. Ap. 7. 845:41

Battisti AJ, Calzetti D, Chary R-R. 2016. Ap. 7. 818:13

Battisti AJ, Calzetti D, Chary R-R. 2017a. Ap. 7. 840:109

Battisti AJ, Calzetti D, Chary R-R. 2017b. Ap. 7. 851:90

Battisti AJ, da Cunha E, Shivaei I, et al. 2020. Ap. 7. 888:108

Berlind AA, Quillen AC, Pogge RW, et al. 1997. Astron. J. 114:107-14

Berry M, Ivezić Ž, Sesar B, et al. 2012. Ap. 7. 757:166

Bianchi S, Clayton GC, Bohlin RC, et al. 1996. Ap. 7. 471:203-10

Bianchi S, Ferrara A, Davies JI, et al. 2000. MNRAS 311:601-10

Blitz L, Shu FH. 1980. Ap. 7. 238:148-57

Boissier S, Gil de Paz A, Boselli A, et al. 2007. Ap. J. Suppl. 173:524-37

Boquien M, Buat V, Boselli A, et al. 2012. Astron. Astrophys. 539:A145

Boquien M, Burgarella D, Roehlly Y, et al. 2019. Astron. Astrophys. 622:A103

Boquien M, Calzetti D, Kennicutt R, et al. 2009. Ap. J. 706:553-70

Bourne N, Dunlop JS, Merlin E, et al. 2017. MNRAS 467:1360-85

Bouwens RJ, Aravena M, Decarli R, et al. 2016. Ap. 7. 833:72

Brammer GB, van Dokkum PG, Franx M, et al. 2012. Ap. 7. Suppl. 200:13

Buat V, Giovannoli E, Heinis S, et al. 2011. Astron. Astrophys. 533:A93

Buat V, Iglesias-Páramo J, Seibert M, et al. 2005. Ap. J. Lett. 619:L51-54

Buat V, Noll S, Burgarella D, et al. 2012. Astron. Astrophys. 545:A141

Burgarella D, Buat V, Iglesias-Páramo J. 2005. MNRAS 360:1413-25

Calzetti D. 1997. Astron. 7. 113:162-84

Calzetti D. 2001. Publ. Astron. Soc. Pac. 113:1449-85

Calzetti D, Armus L, Bohlin RC, et al. 2000. Ap. 7. 533:682-95

Calzetti D, Kinney AL, Storchi-Bergmann T. 1994. Ap. J. 429:582-601

Capak PL, Carilli C, Jones G, et al. 2015. Nature 522:455-58

Cardelli JA, Clayton GC, Mathis JS. 1989. Ap. J. 345:245-56

Casey CM, Narayanan D, Cooray A. 2014a. Phys. Rep. 541:45-161

Casey CM, Scoville NZ, Sanders DB, et al. 2014b. Ap. J. 796:95

Charlot S, Fall SM. 2000. Ap. 7. 539:718-31

Chary R, Elbaz D. 2001. Ap. 7. 556:562-81

Chevallard J, Charlot S, Wandelt B, et al. 2013. MNRAS 432:2061-91

Clayton GC, Gordon KD, Wolff MJ. 2000. Ap. J. Suppl. 129:147–57

Clayton GC, Martin PG. 1985. Ap. 7. 288:558-68

Conroy C. 2010. MNRAS 404:247-52

Conroy C. 2013. Annu. Rev. Astron. Astrophys. 51:393-455

Conroy C, Schiminovich D, Blanton MR. 2010. Ap. 7. 718:184-98

Corre D, Buat V, Basa S, et al. 2018. Astron. Astrophys. 617:A141

Cortese L, Boselli A, Buat V, et al. 2006. Ap. 7. 637:242-54

Cullen F, McLure RJ, Khochfar S, et al. 2017. MNRAS 470:3006–26

da Cunha E, Charlot S, Elbaz D. 2008. MNRAS 388:1595-617

Daddi E, Alexander DM, Dickinson M, et al. 2007. Ap. 7. 670:173-89

Dalcanton JJ, Fouesneau M, Hogg DW, et al. 2015. Ap. 7. 814:3

Dale DA, Cohen SA, Johnson LC, et al. 2009. Ap. 7. 703:517-56

Dale DA, Helou G. 2002. Ap. 7. 576:159-68

Davé R, Anglés-Alcázar D, Narayanan D, et al. 2019. MNRAS 486:2827-49

De Looze I, Fritz J, Baes M, et al. 2014. Astron. Astrophys. 571:A69

De Marchi G, Panagia N, Sabbi E, et al. 2016. MNRAS 455:4373-87

Decleir M, De Looze I, Boquien M, et al. 2019. MNRAS 486:743-67

Desert F-X, Boulanger F, Puget JL. 1990. Astron. Astrophys. 500:313-34

Dong H, Li Z, Wang QD, et al. 2014. Ap. J. 785:136

Dong H, Li Z, Wang QD, et al. 2016. MNRAS 459:2262-73

Draine BT. 2003. Annu. Rev. Astron. Astrophys. 41:241-89

Draine BT. 2004. In *The Cold Universe*, Saas-Fee Advanced Course 32, ed. D Pfenniger, Y Revas, pp. 213–304. Berlin: Springer-Verlag

Draine BT. 2009. In Cosmic Dust—Near and Far, ed. T Henning, E Grün, J Steinacker, ASP Conf. Ser. 414:453–72. San Francisco: ASP

Draine BT. 2011. Physics of the Interstellar and Intergalactic Medium. Princeton, NJ: Princeton Univ. Press

Draine BT, Lee HM. 1984. Ap. J. 285:89-108

Draine BT, Li A. 2007. Ap. 7. 657:810-37

```
Duley WW. 1987. MNRAS 229:203-12
```

Duley WW, Williams DA. 1983. MNRAS 205:67P-70P

Dwek E, Arendt RG, Fixsen DJ, et al. 1997. Ap. 7. 475:565-79

Elmegreen DM, Kaufman M, Elmegreen BG, et al. 2001. Astron. 7. 121:182-97

Erb DK, Steidel CC, Shapley AE, et al. 2006. Ap. 7. 647:128-39

Faber SM. 1972. Astron. Astrophys. 20:361–74

Faber SM, Wegner G, Burstein D, et al. 1989. Ap. J. Suppl. 69:763-808

Faisst AL, Capak PL, Yan L, et al. 2017. Ap. 7. 847:21

Falco EE, Impey CD, Kochanek CS, et al. 1999. Ap. J. 523:617-32

Fanelli MN, O'Connell RW, Thuan TX. 1988. Ap. J. 334:665-87

Ferrara A, Bianchi S, Cimatti A, et al. 1999. Ap. J. Suppl. 123:437-45

Ferrara A, Hirashita H, Ouchi M, et al. 2017. MNRAS 471:5018-24

Fischera J, Dopita M. 2011. Astron. Astrophys. 533:A117

Fitzpatrick EL. 1985. Ap. J. 299:219-35

Fitzpatrick EL. 1999. Publ. Astron. Soc. Pac. 111:63-75

Fitzpatrick EL, Massa D. 1986. Ap. 7. 307:286-94

Fitzpatrick EL, Massa D. 1988. Ap. 7. 328:734-46

Fitzpatrick EL, Massa D. 1990. Ap. J. Suppl. 72:163-89

Fitzpatrick EL, Massa D. 2007. Ap. J. 663:320-41

Fitzpatrick EL, Massa D. 2009. Ap. 7. 699:1209-22

Fontanot F, Somerville RS. 2011. MNRAS 416:2962-73

Fontanot F, Somerville RS, Silva L, et al. 2009. MNRAS 392:553-69

Forrest B, Tran K-VH, Tomczak AR, et al. 2016. Ap. J. Lett. 818:L26

Förster Schreiber NM, Genzel R, Bouché N, et al. 2009. Ap. J. 706:1364-428

Fudamoto Y, Oesch PA, Schinnerer E, et al. 2017. MNRAS 472:483-90

Galliano F, Galametz M, Jones AP. 2018. Annu. Rev. Astron. Astrophys. 56:673–713

Galliano F, Hony S, Bernard J-P, et al. 2011. Astron. Astrophys. 536:A88

Gil de Paz A, Boissier S, Madore BF, et al. 2007. Ap. J. Suppl. 173:185-255

Gillett FC, Jones TW, Merrill KM, Stein WA. 1975. Astron. Astrophys. 45:77-81

Gjergo E, Granato GL, Murante G, et al. 2018. MNRAS 479:2588-606

Goldader JD, Meurer G, Heckman TM, et al. 2002. Ap. 7. 568:651–78

Gonzalez-Perez V, Lacey CG, Baugh CM, Frenk CS, Wilkins SM. 2013. MNRAS 429:1609-25

Gordon KD, Calzetti D, Witt AN. 1997. Ap. 7. 487:625-35

Gordon KD, Clayton GC. 1998. Ap. 7. 500:816-24

Gordon KD, Clayton GC, Misselt KA, et al. 2003. Ap. 7. 594:279–93

Granato GL, Lacey CG, Silva L, et al. 2000. Ap. J. 542:710–30

Grasha K, Calzetti D, Andrews JE, et al. 2013. Ap. J. 773:174

Greenberg JM. 1986. Ap. Space Sci. 128:17-31

Hagen LMZ, Siegel MH, Hoversten EA, et al. 2017. MNRAS 466:4540-57

Heinis S, Buat V, Béthermin M, et al. 2013. MNRAS 429:1113-32

Hirashita H. 2015. MNRAS 447:2937-50

Hirashita H, Aoyama S. 2019. MNRAS 482:2555-72

Holwerda BW, Keel WC, Williams B, et al. 2009. Astron. 7. 137:3000-8

Hou K-C, Aoyama S, Hirashita H, Nagamine K, Shimizu I. 2019. MNRAS 485:1727-44

Howell JH, Armus L, Mazzarella JM, et al. 2010. Ap. 7. 715:572-88

Hoyle F, Wickramasinghe NC. 1969. Nature 223:459-62

Inoue AK. 2005. MNRAS 359:171-82

Inoue AK, Buat V, Burgarella D, et al. 2006. MNRAS 370:380-98

Johnson BD, Leja JL, Conroy C, et al. 2019. Astrophysics Source Code Library. ascl:1905.025

Johnson BD, Schiminovich D, Seibert M, et al. 2007. Ap. 7. Suppl. 173:392–403

Jones AP, Duley WW, Williams DA. 1990. Q. J. R. Astron. Soc. 31:567-82

Jones AP, Köhler M, Ysard N, Bocchio M, Verstraete L. 2017. Astron. Astrophys. 602:A46

Jonsson P, Cox TJ, Primack JR, et al. 2006. Ap. J. 637:255-68

Kauffmann G, Heckman TM, White SDM, et al. 2003. MNRAS 341:33-53

Keel WC, Manning AM, Holwerda BW, et al. 2014. Astron. 7. 147:44

Kemper F, Vriend WJ, Tielens AGGM. 2004. Ap. 7. 609:826-37

Kim S-H, Martin PG, Hendry PD. 1994. Ap. J. 422:164-75

Kinney AL, Bohlin RC, Calzetti D, et al. 1993. Ap. 7. Suppl. 86:5-93

Kinney AL, Calzetti D, Bica E, et al. 1994. Ap. J. 429:172-76

Kong X. Charlot S, Brinchmann J, Fall SM. 2004. MNRAS 349:769-78

Koornneef J, Code AD. 1981. Ap. 7. 247:860-68

Koprowski MP, Coppin KEK, Geach JE, et al. 2018. MNRAS 479:4355-66

Koyama Y, Shimakawa R, Yamamura I, et al. 2019. Publ. Astron. Soc. Jpn. 71:8

Kriek M, Conroy C. 2013. Ap. J. Lett. 775:L16

Kuo T-M, Hirashita H. 2012. MNRAS 424:L34-38

Laor A, Draine BT. 1993. Ap. 7. 402:441-68

Leitherer C, Schaerer D, Goldader JD, et al. 1999. Ap. J. Suppl. 123:3-40

Leja J, Johnson BD, Conroy C, van Dokkum PG, Byler N. 2017. Ap. J. 837:170

Leja J, Johnson BD, Conroy C, et al. 2018. Ap. J. 854:62

Lenz D, Hensley BS, Doré O. 2017. Ap. J. 846:38

Li A, Draine BT. 2001. Ap. J. 554:778-802

Li A, Greenberg JM. 1997. Astron. Astrophys. 323:566-84

Li Q, Narayanan D, Davé R. 2019. MNRAS 490:1425-36

Liang L, Feldmann R, Kereš D, et al. 2019. MNRAS 489:1397-422

Lo Faro B, Buat V, Roehlly Y, et al. 2017. MNRAS 472:1372-91

Ma J, Caucal P, Noterdaeme P, et al. 2015. MNRAS 454:1751-66

Ma J, Ge J, Zhao Y, et al. 2017. MNRAS 472:2196-220

Ma X, Hayward CC, Casey CM, et al. 2019. MNRAS 487:1844-64

Madau P, Dickinson M. 2014. Annu. Rev. Astron. Astrophys. 52:415-86

Malhotra S, Rhoads JE, Turner EL. 1997. MNRAS 288:138-44

Mancini M, Schneider R, Graziani L, et al. 2016. MNRAS 462:3130-45

Mao Y-W, Kong X, Lin L. 2014. Ap. 7. 789:76

Marrone DP, Spilker J, et al. 2018. Nature 553:51-54

Massa D, Fitzpatrick EL. 1986. Ap. J. Suppl. 60:305-21

Massa D, Savage BD, Fitzpatrick EL. 1983. Ap. J. 266:662-83

Mathis JS. 1990. Annu. Rev. Astron. Astrophys. 28:37-70

Mathis JS, Rumpl W, Nordsieck KH. 1977. Ap. 7. 217:425-33

McKinnon R, Torrey P, Vogelsberger M. 2016. MNRAS 457:3775-800

McKinnon R, Vogelsberger M, Torrey P, Marinacci F, Kannan R. 2018. MNRAS 478:2851-86

McLure RJ, Dunlop JS, Cullen F, et al. 2018. MNRAS 476:3991-4006

Meurer GR, Heckman TM, Calzetti D. 1999. Ap. 7. 521:64-80

Meurer GR, Heckman TM, Leitherer C, et al. 1995. Astron. 7. 110:2665-91

Mieda E, Wright SA, Larkin JE, et al. 2016. Ap. 7. 831:78

Misselt KA, Clayton GC, Gordon KD. 1999. Ap. 7. 515:128-39

Motta V, Mediavilla E, Muñoz JA, et al. 2002. Ap. J. 574:719-25

Muñoz JA, Falco EE, Kochanek CS, et al. 2004. Ap. 7. 605:614-19

Nadeau D, Yee HKC, Forrest WJ, et al. 1991. Ap. 7. 376:430-38

Nandy K, Morgan DH, Willis AJ, et al. 1981. MNRAS 196:955-66

Narayanan D, Conroy C, Davé R, Johnson BD, Popping G. 2018a. Ap. 7. 869:70

Narayanan D, Davé R, Johnson BD, et al. 2018b. MNRAS 474:1718-36

Narayanan D, Turk M, Feldmann R, et al. 2015. Nature 525:496-99

Nataf DM, Gonzalez OA, Casagrande L, et al. 2016. MNRAS 456:2692-706

Natale G, Popescu CC, Tuffs RJ, et al. 2015. MNRAS 449:243-67

Noll S, Burgarella D, Giovannoli E, et al. 2009a. Astron. Astrophys. 507:1793-813

```
Noll S, Pierini D, Cimatti A, et al. 2009b. Astron. Astrophys. 499:69–85
Noll S, Pierini D, Pannella M, et al. 2007. Astron. Astrophys. 472:455-69
Nozawa T, Asano RS, Hirashita H, Takeuchi TT. 2015. MNRAS 447:L16-20
O'Donnell JE. 1994. Ap. 7. 422:158–63
Oteo I, Cepa J, Bongiovanni Á, et al. 2013. Astron. Astrophys. 554:L3
Overzier RA, Heckman TM, Wang J, et al. 2011. Ap. 7. Lett. 726:L7
Panuzzo P, Granato GL, Buat V, et al. 2007. MNRAS 375:640-48
Papovich C, Dickinson M, Ferguson HC. 2001. Ap. 7. 559:620–53
Peek JEG, Graves GJ. 2010. Ap. 7. 719:415-24
Peek JEG, Schiminovich D. 2013. Ap. 7. 771:68
Penner K, Dickinson M, Pope A, et al. 2012. Ap. 7. 759:28
Pierini D, Gordon KD, Witt AN, et al. 2004. Ap. 7. 617:1022-46
Pope A, Montaña A, Battisti A, et al. 2017. Ap. 7. 838:137
Popescu CC, Tuffs RJ, Dopita MA, et al. 2011. Astron. Astrophys. 527:A109
Popping G, Puglisi A, Norman CA. 2017a. MNRAS 472:2315-33
Popping G, Somerville RS, Galametz M. 2017b. MNRAS 471:3152–85
Prevot ML, Lequeux J, Maurice E, et al. 1984. Astron. Astrophys. 132:389-92
Price SH, Kriek M, Brammer GB, et al. 2014. Ap. 7. 788:86
Puglisi A, Rodighiero G, Franceschini A, et al. 2016. Astron. Astrophys. 586:A83
Reddy NA, Kriek M, Shapley AE, et al. 2015. Ap. 7. 806:259
Reddy NA, Oesch PA, Bouwens RJ, et al. 2018. Ap. 7. 853:56
Reddy NA, Pettini M, Steidel CC, et al. 2012. Ap. 7. 754:25
Reddy NA, Steidel CC. 2004. Ap. J. Lett. 603:L13-16
Riechers DA, Bradford CM, Clements DL, et al. 2013. Nature 496:329-33
Rieke GH, Lebofsky MJ. 1985. Ap. 7. 288:618-21
Rocha M, Jonsson P, Primack JR, et al. 2008. MNRAS 383:1281-91
Rodighiero G, Daddi E, Baronchelli I, et al. 2011. Ap. J. Lett. 739:L40
Roman-Duval J, Jenkins EB, Williams B, et al. 2019. Ap. 7. 871:151
Sabbi E, Anderson J, Lennon DJ, et al. 2013. Astron. 7. 146:53
Safarzadeh M, Hayward CC, Ferguson HC. 2017. Ap. 7. 840:15
Salim S, Boquien M. 2019. Ap. J. 872:23
Salim S, Boquien M, Lee JC. 2018. Ap. 7. 859:11
Salim S. Charlot S, Rich RM, et al. 2005. Ap. 7. Lett. 619:L39-42
Salim S, Lee JC, Janowiecki S, et al. 2016. Ap. 7. Suppl. 227:2
Salim S, Rich RM, Charlot S, et al. 2007. Ap. 7. Suppl. 173:267–92
Salmon B, Papovich C, Long J, et al. 2016. Ap. 3. 827:20
Savage BD, Mathis JS. 1979. Annu. Rev. Astron. Astrophys. 17:73-111
Sawicki M, Yee HKC. 1998. Astron. 7. 115:1329-39
Schady P, Dwelly T, Page MJ, et al. 2012. Astron. Astrophys. 537:A15
Schlafly EF, Finkbeiner DP. 2011. Ap. 7. 737:103
Schlafly EF, Finkbeiner DP, Schlegel DJ, et al. 2010. Ap. J. 725:1175–91
Schlafly EF, Green G, Finkbeiner DP, et al. 2014. Ap. 7. 789:15
Schlafly EF, Meisner AM, Stutz AM, et al. 2016. Ap. 7. 821:78
Schlegel DJ, Finkbeiner DP, Davis M. 1998. Ap. 7. 500:525-53
Scoville N, Faisst A, Capak P, et al. 2015. Ap. 7. 800:108
Seibert M, Martin DC, Heckman TM, et al. 2005. Ap. J. Lett. 619:L55-58
Seon K-I, Draine BT. 2016. Ap. 7. 833:201
Shapley AE. 2011. Annu. Rev. Astron. Astrophys. 49:525-80
Shivaei I, Reddy NA, Steidel CC, et al. 2015. Ap. J. 804:149
Siana B, Smail I, Swinbank AM, et al. 2009. Ap. 7. 698:1273-81
```

Siebenmorgen R, Kruegel E. 1992. Astron. Astrophys. 259:614–26

Siebenmorgen R, Voshchinnikov NV, Bagnulo S. 2014. Astron. Astrophys. 561:A82

Silva L, Granato GL, Bressan A, et al. 1998. Ap. J. 509:103-17

Somerville RS, Davé R. 2015. Annu. Rev. Astron. Astrophys. 53:51-113

Speagle JS, Steinhardt CL, Capak PL, et al. 2014. Ap. J. Suppl. 214:15

Spinrad H, Taylor BJ. 1971. Ap. J. Suppl. 22:445-84

Stebbins J, Huffer CM, Whitford AE. 1939. Ap. 7. 90:209-29

Stecher TP, Donn B. 1965. Ap. J. 142:1681–82

Steidel CC, Rudie GC, Strom AL, et al. 2014. Ap. 7. 795:165

Steinacker J, Baes M, Gordon KD. 2013. Annu. Rev. Astron. Astrophys. 51:63-104

Strandet ML, Weiss A, De Breuck C, et al. 2017. Ap. 7. Lett. 842:L15

Stratta G, Maiolino R, Fiore F, et al. 2007. Ap. 7. Lett. 661:L9-12

Takeuchi TT, Buat V, Heinis S, et al. 2010. Astron. Astrophys. 514:A4

Takeuchi TT, Yuan F-T, Ikeyama A, Murata KL, Inoue AK. 2012. Ap. J. 755:144

Trayford JW, Camps P, Theuns T, et al. 2017. MNRAS 470:771-99

Trayford JW, Lagos CDP, Robotham ASG, et al. 2020. MNRAS 491:3937-51

Tress M, Mármol-Queraltó E, Ferreras I, et al. 2018. MNRAS 475:2363-74

Tuffs RJ, Popescu CC, Völk HJ, et al. 2004. Astron. Astrophys. 419:821-35

Valencic LA, Clayton GC, Gordon KD. 2004. Ap. 7. 616:912-24

Viaene S, Baes M, Tamm A, et al. 2017a. Astron. Astrophys. 599:A64

Viaene S, Sarzi M, Baes M, et al. 2017b. MNRAS 472:1286–99

Vijayan AP, Clay SJ, Thomas PA, et al. 2019. MNRAS 489:4072–89

Walcher J, Groves B, Budavári T, Dale D. 2011. Ap. Space Sci. 331:1-52

Wang S, Chen X. 2019. Ap. J. 877:116

Wang W, Kassin SA, Pacifici C, et al. 2018. Ap. 7. 869:161

Weingartner JC, Draine BT. 2001. Ap. 7. 548:296-309

White RE, Keel WC. 1992. Nature 359:129-31

Wiklind T, Dickinson M, Ferguson HC, et al. 2008. Ap. 7. 676:781-806

Wild V, Charlot S, Brinchmann J, et al. 2011a. MNRAS 417:1760-86

Wild V. Groves B. Heckman T. et al. 2011b. MNRAS 410:1593-610

Wilkins SM, Gonzalez-Perez V, Lacey CG, Baugh CM. 2012. MNRAS 424:1522-29

Williams TG, Baes M, De Looze I, et al. 2019. MNRAS 487:2753-70

Witt AN, Gordon KD. 1996. Ap. 7. 463:681-93

Witt AN, Gordon KD. 2000. Ap. J. 528:799-816

Wuyts S, Förster Schreiber NM, Lutz D, et al. 2011. Ap. 7. 738:106

Yanchulova Merica-Jones P, Sandstrom KM, Johnson LC, et al. 2017. Ap. 7. 847:102

York DG, Khare P, Vanden Berk D, et al. 2006. MNRAS 367:945-78

Ysard N, Köhler M, Jones A, et al. 2016. Astron. Astrophys. 588:A44

Yuan HB, Liu XW, Xiang MS. 2013. MNRAS 430:2188-99

Zafar T, Watson D, Fynbo JPU, et al. 2011. Astron. Astrophys. 532:A143

Zafar T, Watson D, Møller P, et al. 2018. MNRAS 479:1542-54

Zeimann GR, Ciardullo R, Gronwall C, et al. 2015. Ap. 7. 814:162

Zubko V, Dwek E, Arendt RG. 2004. Ap. 7. Suppl. 152:211-49

Zhukovska S, Dobbs C, Jenkins EB, Klessen RS. 2016. Ap. 7. 831:147



Annual Review of Astronomy and Astrophysics

Volume 58, 2020

Contents

Jack of All James E. Gunn	1
The Assembly of the First Massive Black Holes Kohei Inayoshi, Eli Visbal, and Zoltán Haiman	27
Spatially Resolved Spectroscopic Properties of Low-Redshift Star-Forming Galaxies Sebastián F. Sánchez	99
The Evolution of the Star-Forming Interstellar Medium Across Cosmic Time Linda J. Tacconi, Reinhard Genzel, and Amiel Sternberg	157
Streams, Substructures, and the Early History of the Milky Way Amina Helmi	205
Intermediate-Mass Black Holes Jenny E. Greene, Jay Strader, and Luis C. Ho	257
Astronomers Engaging with the Education Ecosystem: A Best-Evidence Synthesis Stephen M. Pompea and Pedro Russo	313
The Cosmic Baryon and Metal Cycles Céline Péroux and J. Christopher Howk	363
Magnetohydrodynamics Simulations of Active Galactic Nucleus Disks and Jets Shane W. Davis and Alexander Tchekhovskoy	407
Magnetohydrodynamic Waves in the Solar Corona Valery M. Nakariakov and Dmitrii Y. Kolotkov	441
Observations of Protoplanetary Disk Structures Sean M. Andrews	483
The Dust Attenuation Law in Galaxies Samir Salim and Desika Narayanan	529

Evidence for Initial Mass Function Variation in Massive Early-Type Galaxies	
Russell J. Smith	577
Observations of the Lyman-α Universe Masami Ouchi, Yoshiaki Ono, and Takatoshi Shibuya	617
Star-Forming Galaxies at Cosmic Noon Natascha M. Förster Schreiber and Stijn Wuyts	661
Astrochemistry During the Formation of Stars Jes K. Jørgensen, Arnaud Belloche, and Robin T. Garrod	727
Indexes	
Cumulative Index of Contributing Authors, Volumes 47–58	779
Cumulative Index of Article Titles, Volumes 47–58	782

Errata

An online log of corrections to *Annual Review of Astronomy and Astrophysics* articles may be found at http://www.annualreviews.org/errata/astro